THE GEOLOGICAL SOCIETY OF AMERICA®

Deoxygenation and organic carbon sequestration in the Tethyan realm associated with the middle Eocene climatic optimum

Margot J. Cramwinckel[1,†], Robin van der Ploeg[1,†], Niels A.G.M. van Helmond[1], Niels Waarlo[1], Claudia Agnini[2], Peter K. Bijl[1], Annique van der Boon[1,§], Henk Brinkhuis[1,3], Joost Frieling[1,4], Wout Krijgsman[1], Tamsin A. Mather[4], Jack J. Middelburg[1], Francien Peterse[1], Caroline P. Slomp[1], and Appy Sluijs[1]

[1]*Department of Earth Sciences, Faculty of Geoscience, Utrecht University, 3584 CB Utrecht, Netherlands*
[2]*Department of Geosciences, University of Padova, 35131 Padova, Italy*
[3]*Royal Netherlands Institute for Sea Research (NIOZ), NL-1790 Den Burg, Netherlands*
[4]*Department of Earth Sciences, University of Oxford, Oxford OX1 3AN, UK*

ABSTRACT

The middle Eocene climatic optimum (ca. 40 Ma) stands out as a transient global warming phase of ~400 k.y. duration that interrupted long-term Eocene cooling; it has been associated with a rise in atmospheric CO_2 concentrations that has been linked to a flare-up in Arabia-Eurasia continental arc volcanism. Increased organic carbon burial in the Tethys Ocean has been proposed as a carbon sequestration mechanism to bring the middle Eocene climatic optimum to an end. To further test these hypotheses, we assessed the sedimentary and geochemical expression of the middle Eocene climatic optimum in the northern Peri-Tethys, specifically, the organic-rich Kuma Formation of the Belaya River section, located on the edge of the Scythian Platform in the North Caucasus, Russia. We constructed an age-depth model using nannofossil chronobiostratigraphy. Throughout the studied middle Eocene interval (41.2–39.9 Ma), we documented sea-surface temperatures of 32–36 °C based on the tetraether index of tetraethers consisting of 86 carbons (TEX_{86}), depending on proxy calibration, and during the early middle Eocene climatic optimum, we observed sea-surface warming of 2–3 °C. Despite the proximity of the section to the Arabia-Eurasia volcanic arc, the hypothesized source of volcanic CO_2, we found no evidence for enhanced regional volcanism in sedimentary mercury concentrations. Sedimentary trace-element concentrations and iron speciation indicate reducing bottom waters throughout the middle Eocene, but the most reducing, even euxinic, conditions were reached during late middle Eocene climatic optimum cooling. This apparent regional decoupling between ocean warming and deoxygenation hints at a role for regional tectonics in causing basin restriction and anoxia. Associated excess organic carbon burial, extrapolated to the entire regional Kuma Formation, may have been ~8.1 Tg C yr^{-1}, comprising ~450 Pg C over this ~55 k.y. interval. Combined with evidence for enhanced organic carbon drawdown in the western Peri-Tethys, this supports a quantitatively significant role for the basin in the termination of the middle Eocene climatic optimum by acting as a large organic carbon sink, and these results collectively illustrate that the closing Tethys Ocean might have affected global Paleogene climate. Moreover, this study highlights the importance of the interplay between global climate and regional oceanic gateway evolution in determining local climate and oceanographic change.

INTRODUCTION

As a result of anthropogenic greenhouse gas emissions, Earth's oceans are warming (IPCC, 2019) and acidifying (Doney et al., 2009), and oxygen-deficient areas are expanding (Gruber, 2011; Breitburg et al., 2018). Reconstructing and analyzing periods of greenhouse gas–driven global warmth in the geologic past can uniquely aid our understanding of these processes. In particular, the globally warm Eocene Epoch (56–34 Ma; Cramwinckel et al., 2018; Evans et al., 2018; Westerhold et al., 2020), with its superimposed periods of transient warming, holds clues to the functioning of greenhouse Earth climates (Burke et al., 2018; Hollis et al., 2019). The middle Eocene climatic optimum around 40 Ma (Bohaty et al., 2009) represents such a period of transient warming, but with many questions surrounding its causes and consequences, raising fundamental uncertainties in our understanding of global carbon cycling in the past and present climate system (Sluijs et al., 2013; Henehan et al., 2020).

The middle Eocene climatic optimum stands out as an ~400 k.y. period of transient warming in the middle Eocene (Bohaty and Zachos, 2003; Bohaty et al., 2009; Westerhold and Röhl, 2013), interrupting the long-term Eocene cooling trend (Inglis et al., 2015; Westerhold et al., 2020). Over the past decades, indications of middle Eocene climatic optimum warming have been recorded at an increasing number of localities globally. This includes deep waters in Atlantic, Pacific, and Indian deep ocean sites (Bohaty and Zachos, 2003; Bohaty et al., 2009; Dawber and Tripati, 2011; Edgar et al., 2020). Warming also occurred in surface waters of the Atlantic Ocean (Edgar et al., 2010; Boscolo Galazzo et al., 2014; Cramwinckel et al., 2018, 2020a; Arimoto et al., 2020; Henehan et al., 2020), Pacific Ocean (Bijl et al., 2010; Cramwinckel et al., 2020b; Henehan et al., 2020), and Tethys Ocean (Spofforth et al., 2010; Giorgioni et al., 2019). Reconstructed warming at these sites is on the order of 3–6 °C. Middle Eocene climatic optimum warming was likely driven by increasing atmospheric CO_2 concentrations, as indicated by reconstructions based on stable carbon isotope ratios of alkenones (Bijl et al., 2010) and boron isotope ratios ($\delta^{11}B$) of foraminiferal calcite (Henehan et al., 2020). Global stable carbon isotope ratios ($\delta^{13}C$) of sedimentary carbonate lack a distinct coherent signature during middle Eocene

†Shared first authorship; m.j.cramwinckel@uu.nl (corresponding author); r.vanderploeg@uu.nl.
§Present address: Centre for Earth Evolution and Dynamics (CEED), University of Oslo, N-0315 Oslo, Norway.

GSA Bulletin;
published online 1 September 2022

https://doi.org/10.1130/B36280.1; 6 figures; 4 tables; 1 supplemental file.

climatic optimum warming, indicating that the source of excess carbon had a similar isotopic signature as that of surficial carbon reservoirs (Bohaty et al., 2009). This points to volcanic degassing ($\delta^{13}C$ of ~–5‰) rather than a more ^{13}C-depleted organic-derived carbon source, such as sedimentary organic carbon (C_{org}; $\delta^{13}C$ of ~–20‰ to ~–30‰) or methane ($\delta^{13}C$ ~–30‰ to −60‰; Kump and Arthur, 1999; Dickens, 2001). Although there is no evidence for large igneous province emplacement during the middle Eocene, enhanced volcanism from mid-ocean-ridge or continental arc sources has been proposed as the cause of the middle Eocene climatic optimum CO_2 rise (outlined in Bohaty et al., 2009; van der Ploeg et al., 2018). Simple carbon cycle model simulations constrained by available proxy data indicate a carbon cycle imbalance on the order of 2000–4000 Pg C (Sluijs et al., 2013; van der Ploeg et al., 2018; Henehan et al., 2020). Several tectonics-related carbon release events of roughly middle Eocene age have been identified, including increased Pacific Rim arc volcanism, metamorphic decarbonation associated with Himalayan uplift (Kerrick and Caldeira, 1999), and mid-ocean-ridge volcanism related to East African (Bailey, 1992) or North Atlantic rifting (Mjelde et al., 2008). However, none of these has a well-resolved temporal link to middle Eocene climatic optimum warming. Recently, a continental arc flare-up in Iran related to Arabia-Eurasia convergence has been proposed as a potential source (Kargaranbafghi and Neubauer, 2018; van der Boon et al., 2021), since compilation of radiometric ages of volcanic rocks in the Iran-Azerbaijan region yields a distinct peak in eruption rates around 40 Ma. There is large uncertainty (300–12,500 Pg C) on the amount of carbon released by this middle Eocene volcanism in the Iran region due to the uncertain extent of the volcanic deposits, and the potential for greatly enhanced C release due to interaction with carbonate-rich sediments (van der Boon et al., 2021). Nevertheless, the temporal correlation could indicate a causal connection between Neotethys arc volcanism and the middle Eocene climatic optimum.

The mechanism(s) responsible for subsequent climatic recovery, in the aftermath of the middle Eocene climatic optimum, presumably through atmospheric CO_2 drawdown (Bijl et al., 2010; Sluijs et al., 2013; Henehan et al., 2020), remain(s) similarly enigmatic. Remarkably, the termination of the middle Eocene climatic optimum occurred on a time scale similar to that seen at the Paleocene-Eocene thermal maximum, for which silicate weathering and organic carbon burial were likely important (Ravizza et al., 2001; Pogge von Strandmann, 2021; Papadomanolaki et al., 2022). Osmium isotope compositions of marine sediments (van der Ploeg et al., 2018) and carbon cycle simulations coupled to CO_2 reconstructions (Caves et al., 2016) indicate a weakened silicate weathering feedback during the middle Eocene compared to, e.g., the Neogene and Paleocene. Therefore, it seems difficult to conceive that silicate weathering suddenly increased in strength during the middle Eocene climatic optimum when long-term weatherability of continental rocks was low (Caves et al., 2016; van der Ploeg et al., 2018). Interestingly, the middle Eocene climatic optimum recovery interval at the Alano di Piave section in Italy (central-western Tethys; Luciani et al., 2010; Agnini et al., 2011) records elevated C_{org} content, indicating a potential role for C_{org} burial (Spofforth et al., 2010), although the lack of well-constrained C_{org} accumulation rates, particularly from continental margin sites, hinders quantification of this process on a global scale. Conspicuously, earlier studies also postulated a link between global cooling during the middle–late Eocene (Beniamovski et al., 2003) and Eocene-Oligocene transition (Allen and Armstrong, 2008) and deposition of organic-rich deposits in the epicontinental Peri-Tethys basin to the north of the Tethys Ocean (Sachsenhofer et al., 2018). Of these organic-rich deposits, the regionally widespread middle–late Eocene Kuma Formation can be traced laterally (Fig. 1) to the Aral Sea in the east (Beniamovski et al., 2003), Bulgaria in the west (Krasheninnikov, 1986; Sachsenhofer et al., 2018), and potentially even across the Black Sea to time-equivalent organic-rich sediments in the Ukrainian Carpathians (Hnylko and Hnylko, 2019).

Collectively, several outstanding questions related to the middle Eocene climatic optimum warrant further investigation within the Peri-Tethys region: (1) Was there a causal link between volcanism in the Iran region and middle Eocene climatic optimum greenhouse warming? (2) How were middle Eocene climatic optimum temperature change, ocean deoxygenation, and C_{org} burial temporally and mechanistically related? (3) Did regional enhanced C_{org} burial in the Peri-Tethys contribute to post–middle Eocene climatic optimum carbon drawdown?

To address these questions, we investigated the Peri-Tethyan response to the climatic changes of the middle Eocene climatic optimum in terms of regional temperature, depositional environment, and carbon drawdown. We targeted the organic-rich middle Eocene Kuma Formation in the Belaya River section (Fig. 1; van der Boon et al., 2019; Popov et al., 2019b), located on the edge of the Scythian Platform in the North Caucasus, Russia, and performed a suite of integrated organic and inorganic geochemical, nannofossil, and marine palynological analyses. To explore the potential relation between continental arc volcanism in the Iran-Azerbaijan region and the middle Eocene climatic optimum (van der Boon et al., 2021), we generated sedimentary mercury (Hg) content data—a relatively novel proxy for assessing volcanism in the geologic record that has hitherto been primarily applied to reconstruct large igneous province volcanism (Sanei et al., 2012; Jones et al., 2019), but not yet applied to relatively smaller-scale arc volcanism. To assess climate change and ocean anoxia, we employed lipid biomarker paleothermometry and redox-sensitive trace elements and iron speciation. Finally, to investigate potential carbon burial, we constructed a chronobiostratigraphic age model and integrated lithologic, carbonate, and C_{org} contents, and stable isotope data. We extrapolated our findings for approximate quantification of carbon drawdown throughout the Kuma Formation by using the extensive mapping of this formation in the Peri-Tethys area (Sachsenhofer et al., 2018).

MATERIAL AND METHODS

Geological Setting and Stratigraphy

Our study area was located along the Belaya River in the North Caucasus region of Russia (44.3665°N, 40.1970°E; paleolatitude ~42°N at 40 Ma according to Paleolatitude.org; van Hinsbergen et al., 2015), ~25 km south of the town of Maikop (Fig. 1). The studied section contains a succession of middle–late Eocene sediments divided into the Cherkessk, Keresta, Kuma, and Belaya Glina Formations (Zakrevskaya et al., 2011; Beniamovski, 2012), which were deposited in a continental shelf setting (van der Boon et al., 2019). Here, we defined the base of the section (0 m) as the sharp transition from the green clays of the Cherkessk Formation to the white marls of the Keresta Formation (Fig. 2). The overlying Kuma Formation (~6.8–52 m) is represented by brown organic-rich marls, while the Belaya Glina Formation (~52–112.5 m) is again characterized by white marls. Further upward, the succession continues into the Maikop Series. The Kuma Formation at the Belaya River has been dated as Bartonian in age based on biostratigraphy of planktonic foraminifera (regional Crimea-Caucasus zones PF13–PF14; Beniamovski, 2012) and calcareous nannofossils (zones NP16–NP17/CP14; Martini, 1971; Okada and Bukry, 1980; van der Boon et al., 2019; Popov et al., 2019b), in line with the age range inferred for the Kuma Formation within the broader region (ca. 44–36.5 Ma; Beniamovski et al., 2003). The Kuma Formation is generally inferred to have been deposited under low-oxygen conditions (Beniamovski et al.,

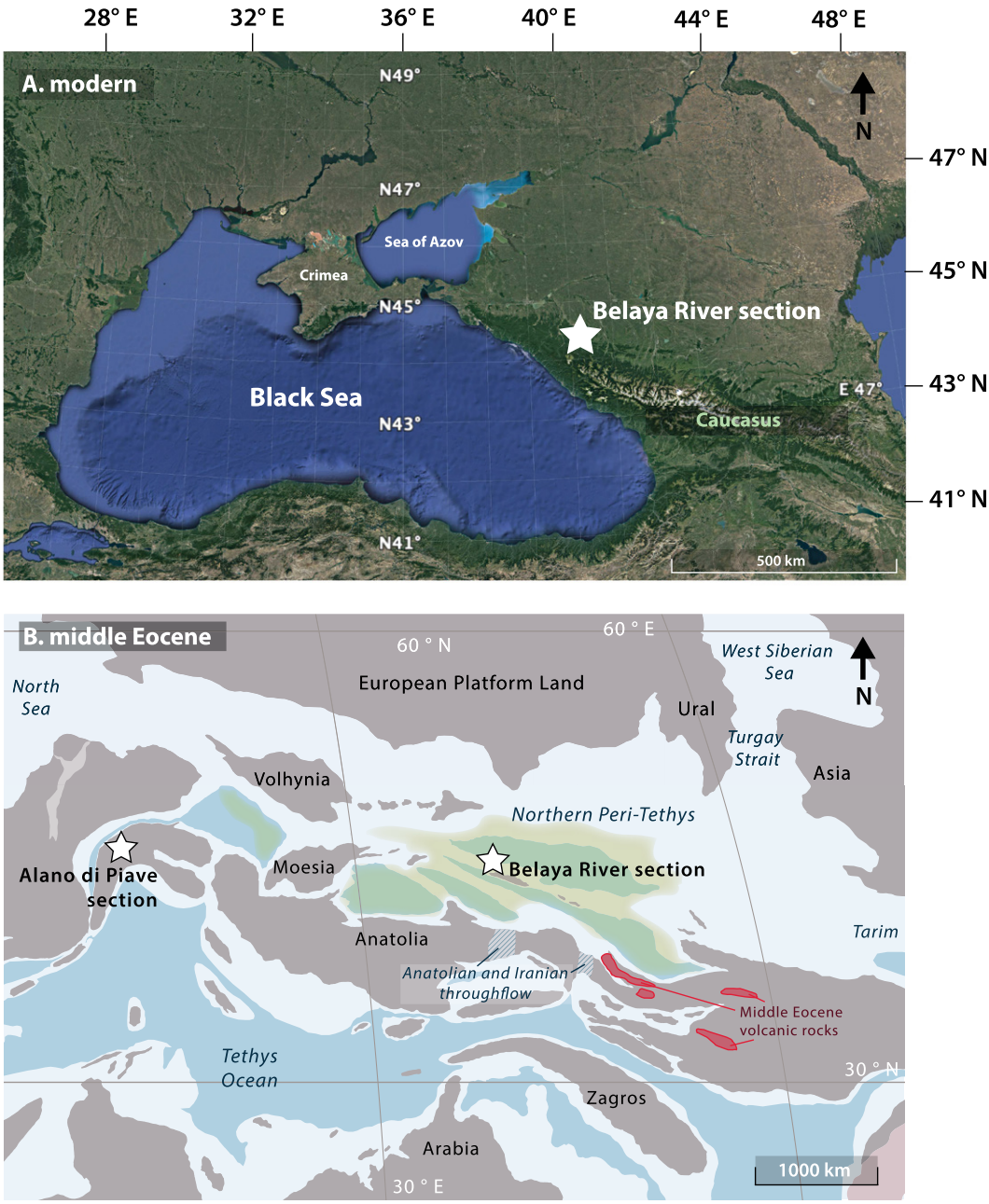

Figure 1. (A) Modern map of the region surrounding the Belaya River section sampling locality (white star). (B) Middle Eocene paleogeographic map of the Tethys region around the Belaya River and Alano di Piave sections (white stars), Modified from the Bartonian (41 Ma) paleogeographic map of Palcu and Krijgsman (2022). Gray shaded areas represent presumed approximate subaerial topography during the middle Eocene. Green shading shows approximate area of Kuma Formation deposits (Sachsenhofer et al., 2018). Red shading shows approximate area of middle Eocene volcanic rocks, as compiled in van der Boon et al. (2021).

2003), as the Peri-Tethys was progressively losing its connectivity to the global ocean (Palcu and Krijgsman, 2022), evolving toward the very restricted Oligocene Paratethys and associated deposition of the organic-rich Maikop Group (Sachsenhofer et al., 2017; Popov et al., 2019a). We targeted the Kuma Formation at the Belaya River section for analysis and the interval between 26 and 37 m in particular, in which the middle Eocene climatic optimum should be expressed under the assumption of continuous sediment accumulation. This interval also contained the darkest-colored and therefore presumably most C_{org}-rich sediments.

Sample Collection

In total, 237 samples (sample codes BX14–BX250) were collected from the Kuma Formation (~6.8–52 m) using a gasoline-powered hand drill during field work in the summer of 2017. The average sampling resolution was chosen at ~10 cm for the interval between 26 and 37 m (suspected middle Eocene climatic optimum interval) and ~30 cm for the rest of the succession. The sample set spanning 20.85–49.55 m (156 samples; BX90–BX245) was selected for subsequent analyses, with the resolution per method chosen depending on the desired scope and available material. To ensure sufficient age-depth constraints, a wider interval (6.86–57.20 m; BX15–BX260) was selected for calcareous nannofossil analysis, encompassing the full Kuma Formation and the lowermost part of the Belaya Glina Formation.

Palynology

For palynological analysis, 40 samples were processed. Between 3 and 10 g (depending on C_{org} content, see section "Organic Carbon, Carbonate, and Nitrogen Contents,

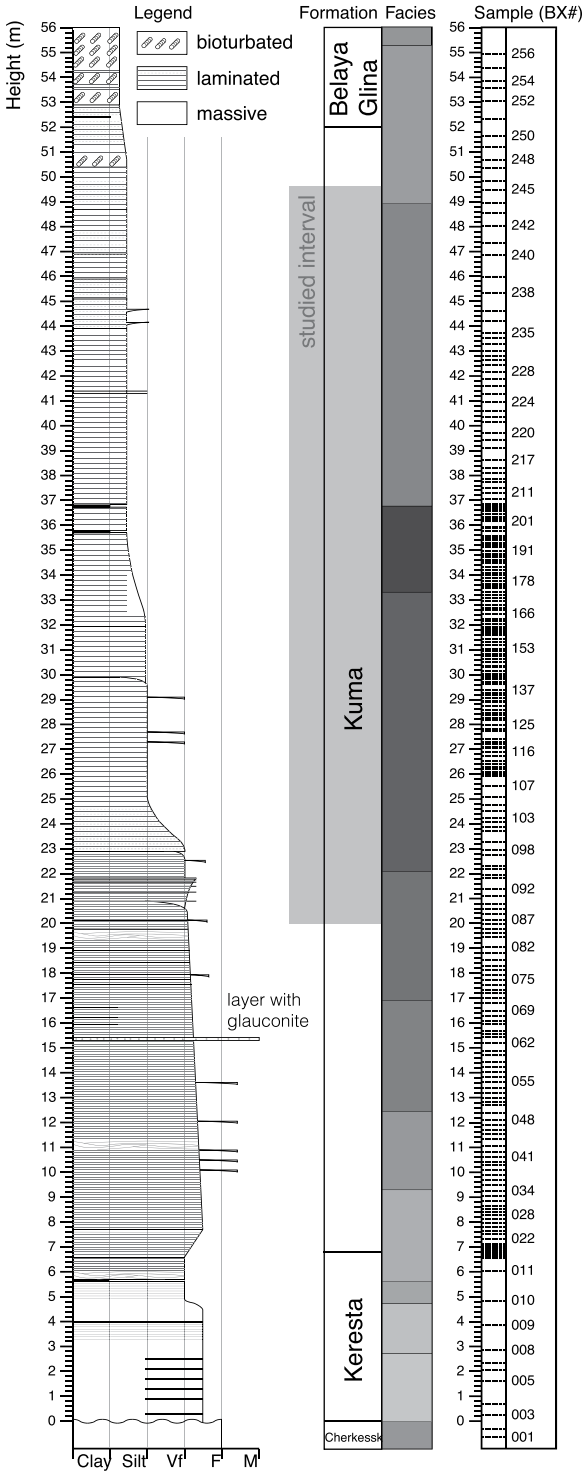

Figure 2. Lithologic log of the Belaya River section (44.3665°N, 40.1970°E), indicating lithology, formations, facies, and samples taken during the summer 2017 expedition. The highlighted studied interval within the Kuma Formation is that studied for geochemistry. Abbreviations: Vf—very fine; F—fine; M—medium.

and Organic Carbon Isotopes") aliquots of freeze-dried, lightly crushed sediment were treated with 30% HCl and ~38%–40% HF to dissolve carbonates and silicates, respectively. The residue was sieved using 15 and 250 μm nylon mesh sieves, with ultrasonic bath steps to break up agglutinated organic matter. The resulting 15–250 μm palynomorph fraction was mounted on glass microscope slides. A general characterization of palynofacies, as well as a scan for stratigraphic marker species of dinoflagellate cysts (dinocysts), was performed with light microscopy, using the taxonomical classification of Williams et al. (2017), with the exception of wetzelielloid taxa (Bijl et al., 2017).

Calcareous Nannofossil Micropaleontology

Calcareous nannofossil analysis was carried out on 43 samples. Samples were prepared as smear slides with standard methods (Bown and Young, 1998) and investigated with light microscopy at a magnification of 1250×. A preliminary qualitative estimation of the abundance and preservation state was performed for all the study samples. The assemblage counts were executed on a minimum of 300 specimens (modified after Thierstein et al., 1977), while for biostratigraphic aims, we counted the number of specimens of the considered taxon present in an area of 1 or 2 mm^2, in the latter case normalized to 1 mm^2 (modified after Backman and Shackleton, 1983). This extension of the counting allowed us to better define the abundance pattern of biostratigraphically important taxa with rare and/or sporadic occurrences that are often not found in standard assemblage counts. The biostratigraphic zonations were adopted from Martini (1971), Okada and Bukry (1980), Fornaciari et al. (2010), and Agnini et al. (2014). The types of biohorizons used were base (B), base common (Bc), top (T), and top common (Tc), as described in Agnini et al. (2014). The taxonomic concepts followed Aubry (1984, 1988, 1989, 1990) and Perch-Nielsen (1985), except for *Dictyococcites* and *Cribrocentrum*, for which we followed Agnini et al. (2014).

Biomarker Geochemistry

Glycerol dialkyl glycerol tetraether (GDGT) lipids were extracted from ~10 g aliquots of powdered, freeze-dried sediment (47 samples) with a Dionex accelerated solvent extractor (ASE 350), using dichloromethane (DCM):methanol (MeOH) (9:1 volume mixture) as solvent. The extracts were separated into apolar, ketone, and polar fractions over an Al_2O_3 column with elution using hexane:DCM (9:1), hexane:DCM (1:1), and DCM:MeOH (1:1), respectively. A known amount of synthetic C_{46} glycerol trialkyl glycerol tetraether (GTGT) standard was added to the polar fraction, which was subsequently dried, redissolved in hexane:isopropanol (99:1), and filtered over a 0.45 μm polytetrafluoroethylene filter to a concentration of ~3 mg mL^{-1}. The GDGT-containing filtrate was analyzed using ultrahigh-performance liquid chromatography–mass spectrometry (UHPLC-MS) on an Agilent 1260 Infinity series high-performance liquid chromatography system coupled to an Agilent 6130 single-quadrupole mass spectrometer in selected ion monitoring mode at Utrecht University, Utrecht, Netherlands. Chromatographic separation of target compounds

was achieved on two Waters BEH HILIC silica columns (2.1 × 150 mm, 1.7 μm) preceded by a guard column (2.1 × 5 mm, Waters) packed with the same material. Solvents, elution scheme, and instrument settings were conducted according to Hopmans et al. (2016). We scanned the resulting chromatograms for presence of isoprenoid GDGTs (isoGDGTs) and branched GDGTs (brGDGTs) (Schouten et al., 2013), but also the more recently recognized branched glycerol monoalkyl glycerol tetraethers (brGMGTs, or H-shaped brGDGTs; Liu et al., 2012; Naafs et al., 2018; Baxter et al., 2019). Tetraether index of tetraethers consisting of 86 carbons (TEX_{86}) values were calculated from isoGDGT abundances following Schouten et al. (2002) and converted to sea-surface temperature (SST) using both an exponential (Kim et al., 2010;) and a linear (O'Brien et al., 2017) calibration. Based on long-term observation of the in-house standard, the analytical precision for TEX_{86} is ±0.3 °C. GDGT abundances (peak areas) are provided in the Supplemental Material[1], in order to facilitate recalculation of SSTs from our GDGT data using any different calibration.

Bulk Carbonate Stable Isotopic Composition

For measurements of the bulk carbonate oxygen and stable carbon isotope ratios ($\delta^{18}O_{carb}$ and $\delta^{13}C_{carb}$), powdered freeze-dried sediments were analyzed using a Thermo Finnigan GasBench-II carbonate preparation device coupled to a Thermo Finnigan Delta-V isotope ratio mass spectrometer (IRMS) at Utrecht University, aiming for 50–100 μg of carbonate per measurement. Analytical errors were ±0.1‰ for $\delta^{13}C$ and $\delta^{18}O$ based on long-term reproducibility of in-house carbonate standards. Values are reported relative to the Vienna Peedee belemnite (VPDB) standard.

[1]Supplemental Material. Figure S1: Abundances of key calcareous nannofossil index taxa throughout the studied interval at the Belaya River section. Figure S2: Mercury (Hg) contents of middle Eocene Belaya River section sediments, plotted together with data sets with comparable C_{org} content. Figure S3: Frequency (number of samples) histogram of binned Hg (ppb)/C_{org} (wt%) values. Table S1: GDGT distributions (peak areas) from the middle Eocene Kuma Formation, Belaya River section. Table S2: Geochemical proxy records from the middle Eocene Kuma Formation, Belaya River section. Table S3: Calcareous nannofossil biostratigraphic data for selected taxa from the middle Eocene Kuma Formation, Belaya River section. Please visit https://doi.org/10.1130/GSAB.S.20371764 to access the supplemental material, and contact editing@geosociety.org with any questions.

TABLE 1. SEQUENTIAL IRON EXTRACTION SCHEME APPLIED IN THIS STUDY, FOLLOWING POULTON AND CANFIELD (2005)

Extraction step	Target phase (minerals)	Fraction
1 mol L^{-1} Na-acetate/acetic acid, pH 4.5 | 24 h	Carbonate-associated Fe (e.g. siderite, ankerite)	Fe_{carb}
1 mol L^{-1} hydroxylamine–HCl solution 25% v/v acetic acid | 48 h	Easily reducible Fe-oxide minerals (e.g. ferrihydrite, lepidocrocite)	Fe_{ox1}
0.35 mol L^{-1} acetic acid/0.2 mol L^{-1} Na_3-citrate/50 g L^{-1} Na-dithionite, pH 4.8 | 2 h	Crystalline Fe-oxide minerals (e.g. goethite, hematite)	Fe_{ox2}
0.17 mol L^{-1} NH_4 oxalate/0.2 mol L^{-1} oxalic acid, pH 3.2 | 6 h	Recalcitrant Fe-oxide minerals (e.g. magnetite)	Fe_{mag}

Organic Carbon, Carbonate, and Nitrogen Contents, and Organic Carbon Isotopes

In order to analyze the elemental composition and carbon isotopes of organic matter ($\delta^{13}C_{org}$), 0.2–0.3 g aliquots of powdered freeze-dried weighted sediment were decalcified using 1 *M* HCl. Residues were oven-dried at 60 °C and weighed again to obtain approximate $CaCO_3$ weight percentages. Total nitrogen (N) and C_{org} contents, as well as stable carbon isotopic ratios of C_{org} ($\delta^{13}C_{org}$), were determined using a Thermo Scientific Flask 2000 elemental analyzer coupled to a Thermo Scientific Delta V Advantage via a Conflo IV elemental analyzer–isotope ratio mass spectrometer (EA-IRMS). Analytical errors were <0.1 wt% for C_{org}, <0.02 wt% for N, and ~0.1‰ for $\delta^{13}C_{org}$ based on long-term reproducibility of in-house standards. Values are reported relative to the VPDB standard.

Total Elemental Composition

To determine elemental composition, for each sample, ~125 mg aliquots of powdered freeze-dried sediment were weighed in Teflon vessels, after which 2.5 mL of 40% HF and 2.5 mL of mixed acid ($HClO_4$:HNO_3, 3:2) were added. Subsequently, the vessels were closed and left overnight on a hotplate at 90 °C. The next day, the lids were removed, and the temperature of the hotplate was increased to 140 °C to fume off the acids. After ~4 h, the remaining residues were dissolved in 25 mL of 4.5% HNO_3 and left overnight on the hotplate at 90 °C. The next day, the vessels were left to cool down to room temperature (~20 °C), after which they were weighed to determine the dilution. The extracts were analyzed by inductively coupled plasma–optical emission spectrometry (ICP-OES; SPECTRO ARCOS). Accuracy (recovery) was at least 95%, and average analytical uncertainty was at most 5% for the elements studied here, based on duplicates and laboratory reference material (ISE-921).

Sequential Extraction of Iron

Subsamples for sedimentary Fe speciation analysis were taken during the Belaya River field campaign and stored under an oxygen-free atmosphere. In the laboratory at Utrecht University, these subsamples were freeze-dried and then powdered in an argon gas–filled glovebox. Between 50 and 80 mg aliquots of powdered sample material were weighed in centrifuge tubes and sequentially extracted (Table 1) following the method presented by Poulton and Canfield (2005). The entire extraction procedure (freeze-drying, powdering, extraction) was conducted under oxygen-free conditions. The Fe content in all extracts was determined colorimetrically using the 1,10-phenanthroline method (APHA, 2005). Average analytical uncertainty, based on duplicates, was <1 μmol/g for Fe_{carb}, Fe_{ox1}, and Fe_{mag} and 6 μmol/g for Fe_{ox2} (Table 1). To determine the amount of Fe present in pyrite, the diffusion method given by Burton et al. (2008) was used. Between 250 and 400 mg aliquots of the anoxic, powdered and freeze-dried sediment were weighed in centrifuge tubes in an argon gas–filled glovebox. Subsequently, 10 mL of acidic chromium(II) chloride was added, while at the same time, a smaller centrifuge tube, containing 7 mL of alkaline zinc acetate solution, was placed in the centrifuge tube holding the sediment sample. The produced sulfide gas was then trapped in the alkaline zinc acetate solution, forming a precipitate of zinc sulfide. The amount of sulfur in the precipitates, i.e., chromium-reducible sulfur (CRS; generally assumed to represent pyrite, i.e., FeS_2), was then determined by iodometric titration (APHA, 2005). Average analytical uncertainty, based on duplicates, was ~20 μmol/g. The highly reactive Fe fraction (Fe_{HR}) was determined by summing the different fractions of the sequential Fe extraction (i.e., Fe_{carb}, Fe_{ox1}, Fe_{ox2}, and Fe_{mag}), and the Fe associated with CRS, i.e., Fe_{py}, was determined by dividing the amount of CRS by two.

Mercury Contents

For analysis of Hg contents, samples were prepared following the protocol described in Percival et al. (2017). Hg contents were measured using a Lumex RA-915 portable mercury analyzer paired with a PYRO-915 pyrolysis unit at the University of Oxford. Hg is reported both as concentrations and normalized to our measured C_{org} contents,

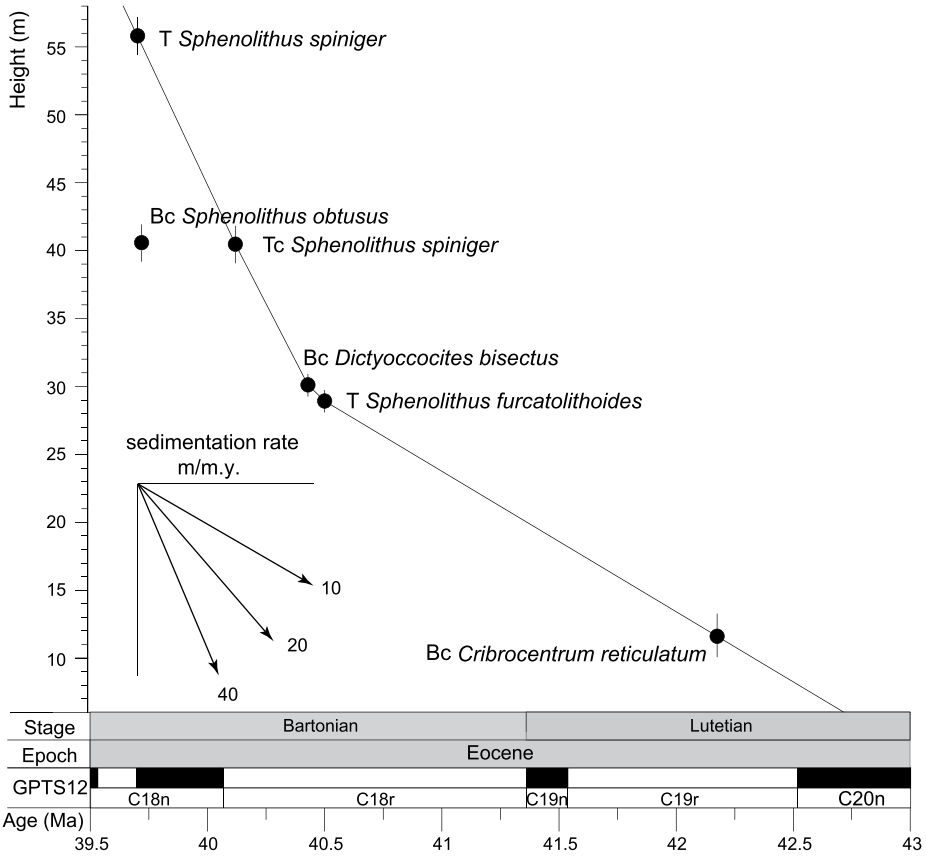

Figure 3. Calcareous nannofossil–based age-depth model of the middle Eocene of the Belaya River section. Age-depth plot shows calcareous nannofossil tie points as presented in Table 2. B, Bc, T, and Tc—base, base common, top, and top common, respectively. GPTS12—Geomagnetic Polarity Time Scale 2012 (Gradstein et al., 2012).

as organic matter is generally assumed to be the most common Hg-binding sedimentary component (Sanei et al., 2012). Comparison with a high-mercury (290 ppb) paint-contaminated soil standard (National Institute of Standards and Technology NIST 2587) showed that typical analytical uncertainty was below 10%.

RESULTS

Palynofacies and Palynological Assemblages

The palynofacies of all samples is dominated by poorly preserved, dark-colored, amorphous organic matter and algal- and plant-derived debris. Sparse palynomorphs include prasinophytes (e.g., *Tasmanites* and *Cymatiosphaera*), organic-walled dinoflagellate cysts (or dinocysts), and sporomorphs. Unfortunately, poor preservation of the material in combination with huge dilution by amorphous organic material hampered determination to the species level, and hence limited use for biostratigraphy. Because of this, we did not perform full quantitative palynological counts, but rather we performed a qualitative characterization of the assemblage. Dominant dinocyst taxa comprising a large part of the assemblages were *Enneadocysta* spp., *Spiniferites* spp., *Cordosphaeridium* spp., *Cleistosphaeridium* spp., *Batiacasphaera* spp., *Hystrichokolpoma* spp., and some Protoperidinioids and wetzelielloids. Peridinioid dinocysts were overall low in abundance relative to gonyaulacoid. The observed combination of taxa is indicative of a middle-shelf, middle Eocene setting (Pross and Brinkhuis, 2005; Sluijs et al., 2005; Frieling and Sluijs, 2018).

Calcareous Nannofossil–Based Biostratigraphy

Since calcareous nannofossils are generally abundant throughout the studied section, showing high diversity and mostly good preservation, they formed the primary basis for our age model (Fig. 3; Table 2). Abundance patterns of index species are provided in Supplemental Figure S1 (see footnote 1). We used the biohorizons from the standard calcareous nannofossil biozonations of Martini (1971) and Okada and Bukry (1980) where possible. However, due to the low reproducibility and reliability of some of these biozonations when applied to the Belaya River section, we integrated the standard framework with the biozonation schemes of Fornaciari et al. (2010; Mediterranean Nannoplankton Paleogene [MNP] zones) and Agnini et al. (2014; Calcareous Nannofossil Eocene [CNE] zones), as listed below from old to young.

Calcareous Nannofossil Biozonation

According to Backman (1987), the top of *Nannotetrina* spp. is marked by the top of *Nannotetrina cristata* and lies in the lowermost part of zone NP16 or subzone CP14a, close to the Bc (base common) of *Reticulofenestra umbilicus* (Agnini et al., 2014). In the Belaya River section, two specimens of *Nannotetrina alata* group (gr.) were observed in the lower part of the succession, but no forms ascribable to *N. cristata* were observed. The presence of very sporadic *N. alata* gr. and the absence of *N. cristata* suggest that the specimens observed have been reworked. This idea is also supported by the presence of other reworked taxa, and therefore we did not use this biohorizon in our age-depth model. The Bc of *Cribrocentrum reticulatum* is used to define the base of zone CNE14 and usually lies within chron

TABLE 2. NANNOFOSSIL-BASED DATUMS USED AS AGE-DEPTH TIE POINTS FOR THE MIDDLE EOCENE BELAYA RIVER SECTION IN THIS STUDY

Event	Species	Biozone (base)	Top (m)	Base (m)	Mid (m)	Sample top	Sample base	Age GTS12 (Ma)	Reference
T	*Sphenolithus spiniger*		57.20	54.45	55.83	BX 260	BX 255	39.72	Fornaciari et al. (2010)
Bc	*Sphenolithus obtusus*	MNP17A	41.35	39.76	40.56	BX 225	BX 220	39.72	Fornaciari et al. (2010)
Tc	*Sphenolithus spiniger*	MNP16Bc	41.35	39.76	40.56	BX 225	BX 220	40.12	Fornaciari et al. (2010)
Bc	*Dictyoccocites bisectus*	CNE15–MNP16Bb	30.35	29.88	30.12	BX 145	BX 140	40.35	Agnini et al. (2014)
T	*Sphenolithus furcatolithoides*	MNP16Ba	29.22	28.65	28.935	BX 135	BX 130	40.48	Agnini et al. (2014)
B	*Sphenolithus predistentus*		26.15	24.83	25.49	BX 110	BX 105		
Bc	*Cribrocentrum reticulatum*	CNE14	12.75	10.47	11.61	BX 50	BX 40	42.15	Agnini et al. (2014)
T	*Nannotetrina* spp.		–	–	–	–	–	42.69	Agnini et al. (2014)

Note: Ages of the tie points were recalibrated to Geologic Time Scale 2012 (GTS2012; Gradstein et al., 2012). T—top; B—base; Tc—top common; Bc—base common.

C19r (Agnini et al., 2014). In the studied succession, *C. reticulatum* appears (base) from sample BX 50 (stratigraphic position 12.75 m) and increases upward in abundance (Fig. S1). The base of *Sphenolithus predistentus* is reported in the upper part of zone CNE14, and the abundance pattern in the study succession from sample BX 110 (stratigraphic position 26.15 m) precedes the base of *D. bisectus*, as previously observed in other publications (Fornaciari et al., 2010; Toffanin et al., 2011; Agnini et al., 2014). Unfortunately, the precise positioning of this biohorizon is difficult to define because of the scattered abundance of the taxon close to its appearance and the presence of transitional forms. At low to midlatitudes, the top of *Sphenolithus furcatolithoides* is used to define the base of subzone MNP16Ba and is consistently found in the upper part of zone CNE14 (Agnini et al., 2014) and the middle-upper part of chron C18r (Fornaciari et al., 2010). In the Belaya River section, *S. furcatolithoides* shows a continuous abundance pattern up to sample BX 135 (stratigraphic position 29.22 m), where it disappears (Fig. S1). The Bc of *Dictyoccocites bisectus* has been used as base of zone CNE15 and of subzone MNP16Bb. This taxon has been characterized by an ambiguous taxonomy (Wei and Wise, 1989); however, recent clarification (long axis >10 μm) has pointed out quite a consistent and reliable position (upper part of chron C18r) for its first occurrence (Fornaciari et al., 2010; Agnini et al., 2014). In the Belaya River section, the base of *D. bisectus* has been observed at sample BX 145 (stratigraphic position 30.35 m; Fig. S1). The Tc (top common) of *Sphenolithus spiniger* marks the base of subzone MNP16Bc (Fornaciari et al., 2010). In the study section, *S. spiniger* displays a continuous pattern and relatively high abundance up to sample BX 225 (stratigraphic position 41.35 m), where it decreases significantly (Tc), but the final extinction does not occur before the last investigated sample (BX 260, stratigraphic position 57.20 m; Fig. S1). The base of *S. obtusus* serves to define the base of subzone MNP17A, although this event is not always found to be synchronous (Fornaciari et al., 2010), possibly due to sporadic occurrences close to its first appearance (e.g., Toffanin et al., 2013). In the Belaya River section, *S. obtusus* is sporadic from BX 150 up to sample BX 225 (stratigraphic position 41.35 m), where it increases in abundance and is continuously present (Bc; Fig. S1). The recognition of the Bc of *S. obtusus* and the Tc of *S. spiniger* invalidates the subzone MNP17A. In order to use the biozonation of Fornaciari et al. (2010), we decided to merge subzones MNP17A and MNP16Bc.

Age-Depth Model

An earlier study indicated that the Kuma Formation sediments at the Belaya River section have a very weak magnetic signal, prohibiting reliable polarity determination and thus magnetostratigraphy (van der Boon et al., 2019). As dinocyst identification was generally not possible to the species level, our age model was based primarily on calcareous nannofossil biostratigraphy and biochronology. Based on the above discussion of nannofossil datums, the tie points that constrained our age model were: the Bc of *C. reticulatum*, the top of *S. furcatolithoides*, the base of *D. bisectus*, and the top and Tc of *S. spiniger* (Fig. 3; Table 2). The base of *S. obtusus* was not used because of the previously discussed low reliability of this biohorizon. Biochronological estimates were recalibrated against the Geologic Time Scale 2012 (GTS12; Gradstein et al., 2012). The age of the base (42.7 Ma) and the top (39.7 Ma) of the section were extrapolated assuming linear sedimentation rates. This implies that the section encompasses ~3 m.y., partially covering the Lutetian and Bartonian and including the middle Eocene climatic optimum, which is in line with earlier work based on multiple groups of microfossils (Popov et al., 2019b). Our chronology indicates that the middle Eocene climatic optimum at the Belaya River section is complete, within the limits of the biozones. Based on average sedimentation rates in between age-depth tie points, this section is characterized by lower sedimentation rates in the older interval (6.86–30.12 m), with values of 9.3–10.3 m/m.y. Sedimentation rates are much higher in the upper part of the section, increasing almost fivefold to 45.7 m/m.y. from Bc *D. bisectus* (40.35 Ma) upward. In the uppermost part of the section (40.56–57.2 m), the average sedimentation rate remains high but slightly decreases to 38.4 m/m.y. This results in an average sampling resolution of ~6 k.y. for the suspected middle Eocene climatic optimum interval (sample spacing ~10 cm) and ~15 k.y. for the surrounding interval (sample spacing ~30 cm). Dinocysts present in our palynological slides support the nannofossil-based Lutetian–Bartonian age constraints, but they do not provide any additional precise age-depth information.

Biomarker Geochemistry: Glycerol Dialkyl Glycerol Tetraethers

GDGT fractions of the Kuma Formation consist almost entirely of isoGDGTs, with brGDGTs being fully absent and brGMGTs being present in low amounts. Several indicator ratios were calculated to appraise isoGDGT sourcing. The methane index (MI; Zhang et al., 2011), GDGT-2/crenarchaeol (Weijers et al., 2011), and GDGT-0/crenarchaeol (Blaga et al., 2009), used to investigate contributions by methanotrophic and methanogenic isoGDGT producers, were all within the ordinary range for production by marine Thaumarchaeota (Supplemental Material), supporting the use of TEX_{86} as SST proxy. Next to this, the relative abundance of crenarchaeol regio-isomer ($f_{Cren':Cren'+Cren}$; O'Brien et al., 2017) and the ring index (RI; Zhang et al., 2016) were assessed to identify anomalous GDGT distributions. Two samples were discarded, as ΔRI was higher than 0.3 (Supplemental Material). Because brGDGTs were entirely below detection limit, resulting branched versus isoprenoid tetraether (BIT) index values, a measure for terrestrially derived GDGTs relative to marine-produced GDGTs (Hopmans et al., 2004; Zell et al., 2013), were 0. Notably, ratios between GDGT-2/GDGT-3 ([2]/[3]; Taylor et al., 2013) were high throughout the record, fluctuating above (12 samples) and below the threshold value of 5.0 that was suggested to indicate isoGDGT contributions by deeper-dwelling marine Archaea. TEX_{86} values ranged between 0.76 and 0.86, recording gradual warming followed by more rapid cooling (Fig. 4). This resulted in a range of reconstructed SSTs between 30.6 °C and 34.2 °C using an exponential calibration (Kim et al., 2010; calibration standard error ±2.5 °C), and a much higher range of 33.8–39.5 °C using a linear calibration (O'Brien et al., 2017; calibration standard error ±2.0 °C).

Despite the absence of brGDGTs, structurally related brGMGTs were detected in the Belaya River section, at around 1%–2% of total GDGTs. BrGMGTs are characterized by an additional covalent bond between the alkyl chains that is thought to be an adaptation to maintain membrane stability under heat stress (Morii et al., 1998). Indeed, the abundance of brGMGTs relative to that of brGDGTs increases with temperature in peats and lake sediments (Naafs et al., 2018; Baxter et al., 2019, 2021). In the Kuma Formation, two isomers, i.e., H1020a and H1020b (nomenclature following Baxter et al., 2019), of the brGMGT labeled as H-1020 in Liu et al. (2012) and Naafs et al. (2018) were reliably detected in all samples, without a clear stratigraphic trend in the ratio between the samples.

Paleoclimate Regimes

In order to facilitate a chronological description and discussion of the results, we subdivided our record into paleoclimate regimes, primarily based on the TEX_{86} temperature record and overall lithological changes (Figs. 4 and 5). The TEX_{86} record was characterized by stable background temperatures in regime I transitioning to gradual warming in regime II, which we

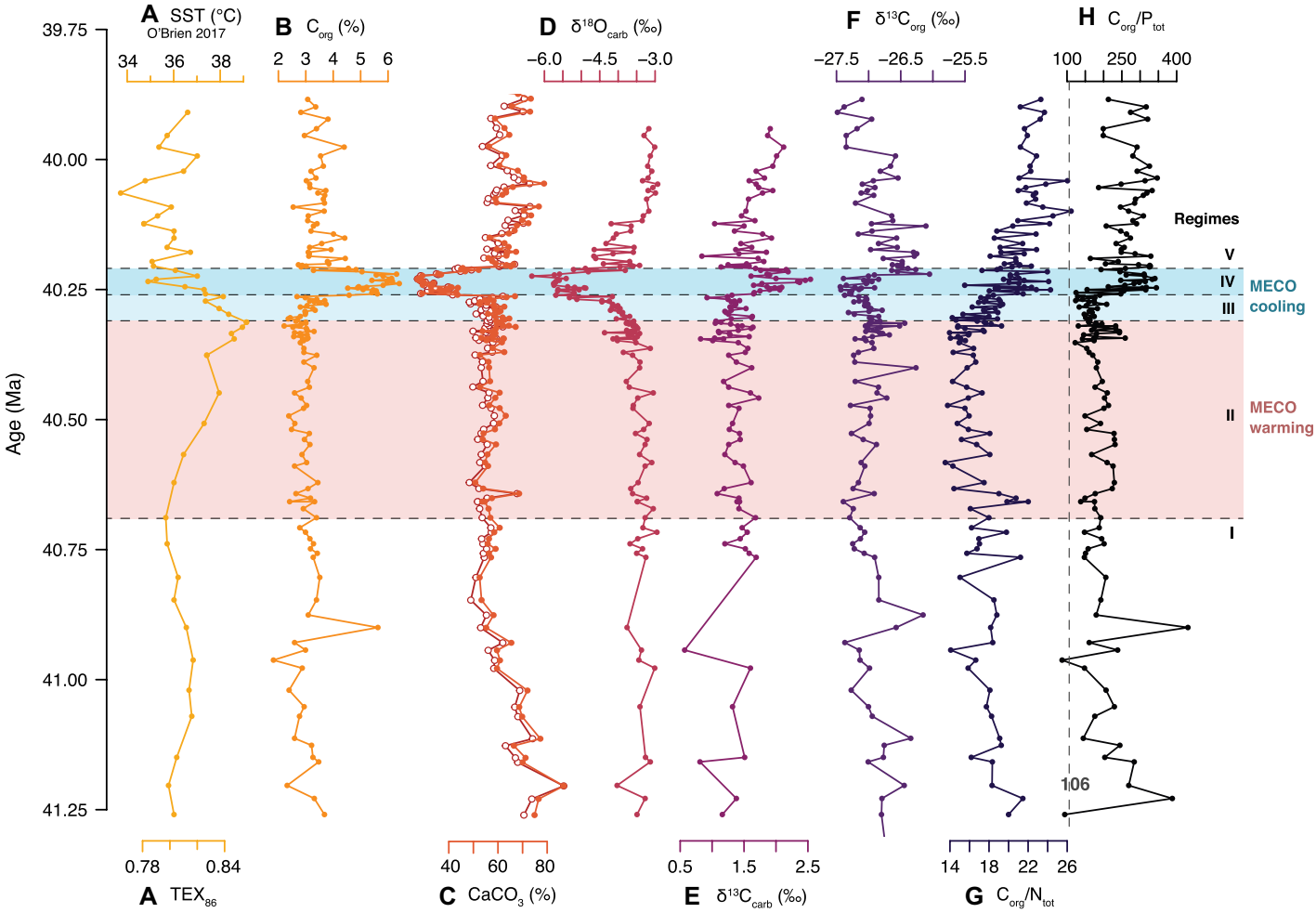

Figure 4. Geochemical proxy records across the middle Eocene climatic optimum interval in the Kuma Formation, Belaya River section, part I. (A) Tetraether index of 86 carbon atoms (TEX_{86}) ratios, converted to sea-surface temperature (SST; in °C) using the linear calibration of O'Brien et al. (2017). (B) Total organic carbon content (C_{org}, in wt%). (C) Total calcium carbonate content ($CaCO_3$, in wt%). Closed symbols are based on weight loss during decalcification. Open symbols were calculated based on Ca from inductively coupled plasma–optical emission spectrometry (ICP-OES), assuming all Ca was in the form of $CaCO_3$. (D) Bulk carbonate $\delta^{18}O$ ($\delta^{18}O_{carb}$, in ‰ relative to Vienna Peedee belemnite [VPDB]). (E) Bulk carbonate $\delta^{13}C$ ($\delta^{13}C_{carb}$, in ‰ VPDB). (F) Organic carbon $\delta^{13}C$ ($\delta^{13}C_{org}$, in ‰ VPDB). (G) C_{org}/N_{tot} ratios (in mol/mol). (H) C_{org}/P_{tot} ratios (in mol/mol), with Redfield ratio (C/P = 106) as vertical dashed line. All records are plotted against age in Geologic Time Scale 2012 (GTS2012; Gradstein et al., 2012) according to the age model presented herein. Horizontal shading was added to represent the different paleoclimate regimes (see "Paleoclimate Regimes" section of the "Results" section), where red and blue colors represent warming and cooling phases, respectively. MECO—middle Eocene climatic optimum.

associate with the onset of the middle Eocene climatic optimum. The interval of subsequent cooling was subdivided into regimes III and IV, in which regime IV was furthermore characterized by a shift in lithology, namely, a sharp drop in carbonate content (Fig. 4). Regime V represents a return to "background" conditions, characterized by more variable temperatures. We note that there is an offset between middle Eocene climatic optimum warming in the Belaya River record as inferred from TEX_{86} (ca. 40.7–40.3 Ma) and the global deep-ocean warming trend (ca. 40.5–40.1 Ma). However, we argue that an ~100–200 k.y. offset is perhaps expected from the current uncertainty in the biostratigraphic reference calibration (see "Calcareous Nannofossil Biozonation" subsection of the "Results" section), combined with our sampling resolution.

Sediment Composition and Geochemistry

General Lithology

Lithology is relatively stable across the studied interval, consisting of bioturbated marls with high carbonate contents (~50%–80%) and relatively high C_{org} contents (~2%–4%; Figs. 4B–4C). The exception to this is regime IV, corresponding approximately to the darkest sedimentary facies, in which $CaCO_3$ drops to ~30% and C_{org} rises to ~6%.

Carbonate Stable Isotope Ratios

Recorded $\delta^{18}O_{carb}$ values (Fig. 4D; Table 3) were overall rather low (–3‰ to –6‰; Fig. 4C; Table 3) compared to contemporaneous open-ocean records (Bohaty et al., 2009). Such values may suggest contributions of diagenetic calcite. However, the preservation of the calcareous nannofossils is remarkably good. These depleted values might also suggest a consistent diagenetic overprint by mete-

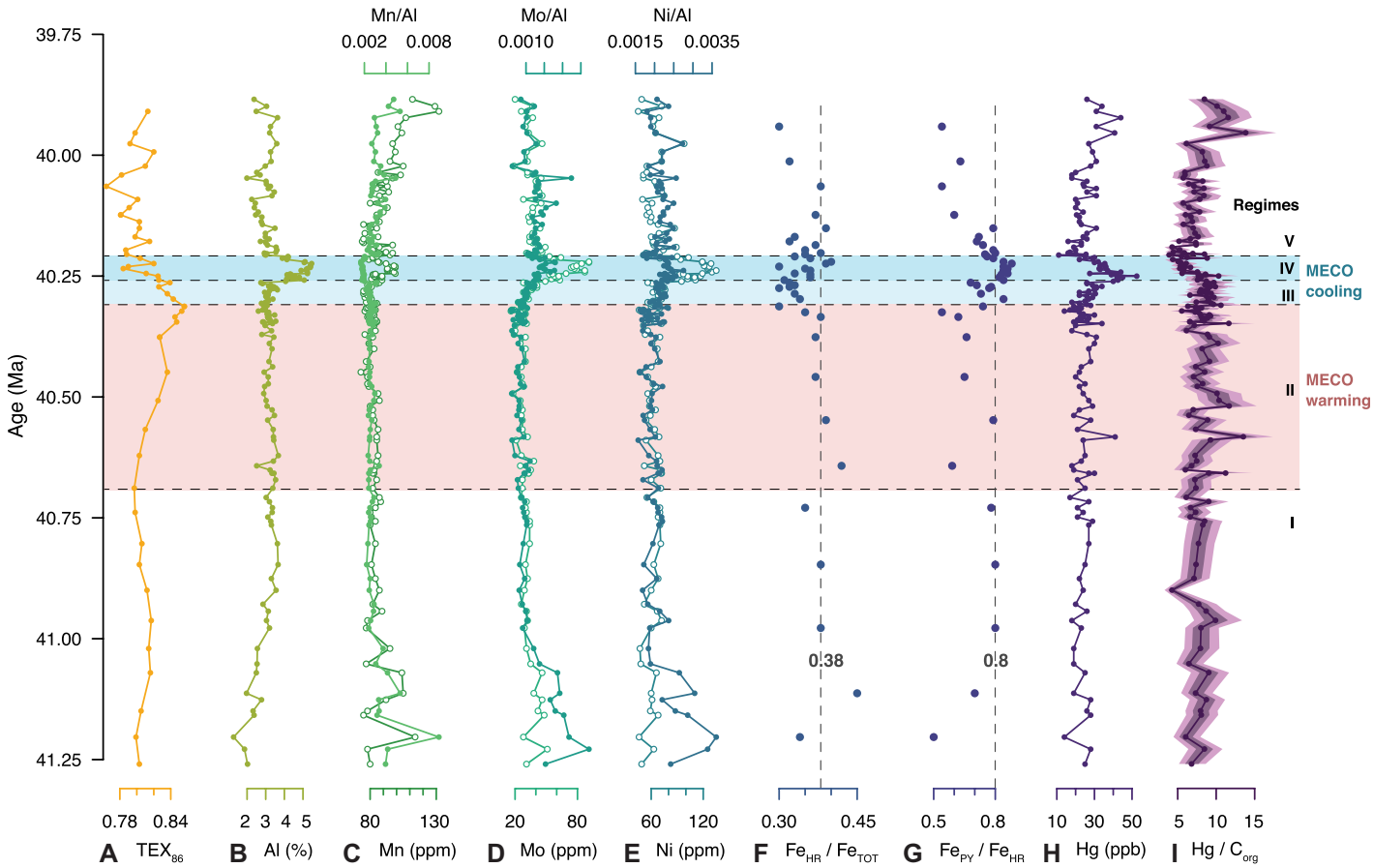

Figure 5. Geochemical proxy records across the middle Eocene climatic optimum interval, Kuma Formation, Belaya River section, part II. (A) Tetraether index of tetraethers consisting of 86 carbons (TEX_{86}) ratios, increasing with increasing sea-surface temperature (SST). (B) Aluminum contents (Al, in %). (C) Manganese (Mn) contents in ppm (dark green, open symbols) and normalized to Al (light green, closed symbols). (D) Molybdenum (Mo) contents in ppm (light turquoise, open symbols) and normalized to Al (dark turquoise, closed symbols). (E) Nickel (Ni) contents in ppm (light blue, open symbols) and normalized to Al (dark blue, closed symbols). (F) Proportion of highly reactive iron (Fe_{HR}) relative to total iron (Fe_{TOT}). (G) Proportion of iron in pyrite (Fe_{PY}) relative to total highly reactive iron (Fe_{HR}). (H) Mercury (Hg) contents in ppb. (I) Hg/C_{org} ratios (in ppb Hg/% C_{org}). Uncertainties plotted are estimated maximum combined analytical uncertainties of Hg/ C_{org}. Darker purple shading is based on Hg – 1 sd and C_{org} + 1 sd (lower end) and Hg + 1 sd and C_{org} – 1 sd (higher end), where sd is standard deviation. Lighter purple shading is based on Hg – 2 sd and C_{org} + 2 sd (lower end) and Hg + 2 sd and C_{org} – 2 sd (higher end). All records are plotted against age in the Geologic Time Scale 2012 (GTS2012; Gradstein et al., 2012) according to the age model presented herein. Horizontal shading was added to represent the different paleoclimate regimes (see "Paleoclimate Regimes" section of the "Results" section). MECO—middle Eocene climatic optimum.

TABLE 3. AVERAGE VALUES FOR SELECTED GEOCHEMICAL PROXIES OVER REGIMES I–V, MIDDLE EOCENE BELAYA RIVER SECTION

	41.26–40.69 (Ma) Pre-MECO background Regime I	40.69–40.31 (Ma) MECO-related warming Regime II	40.31–40.26 (Ma) MECO-related cooling Regime III	40.26–40.21 (Ma) MECO cooling & TOC-rich Regime IV	40.21–39.80 (Ma) Post-MECO background Regime V
TEX_{86}	0.81	0.83	0.84	0.81	0.80
C_{org} (%)	3.1	2.9	3.1	5.4	3.4
$CaCO_3$ (%)	64	59	59	40	64
$\delta^{18}O_{carb}$ (‰ VPDB)	–3.4	–3.5	–4.3	–5.4	–3.6
$\delta^{13}C_{carb}$ (‰ VPDB)	1.3	1.3	1.3	2.0	1.6
$\delta^{13}C_{org}$ (‰ VPDB)	–26.9	–27	–27.1	–27	–26.8
Hg (ppb)	23	24	28	36	25
Hg/C_{org}	7.6	8.3	8.8	6.8	7.3
C_{org}/N_{tot}	18	16	18	21	22
C_{org}/P_{tot}	203	187	162	269	273
Fe_{HR}/Fe_{Tot}	0.38	0.37	0.32	0.35	0.35
Fe_{PY}/Fe_{HR}	0.72	0.66	0.75	0.84	0.70

Note: Cells are shaded per row (variable), with a darker gray representing a higher cell value. MECO—middle Eocene climatic optimum; TOC—total organic carbon; TEX_{86}—tetraether index of tetraethers consisting of 86 carbons; VPDB—Vienna Peedee belemnite; Fe_{HR}—highly reactive iron species; Fe_{PY}—iron in pyrite; org—organic; carb—carbonate; Tot—total.

TABLE 4. AVERAGE VALUES FOR SELECTED REDOX-SENSITIVE TRACE ELEMENTS MEASURED IN THIS STUDY FROM THE BELAYA RIVER SECTION

	41.26–40.69 (Ma) Pre-MECO background Regime I	40.69–40.31 (Ma) MECO-related warming Regime II	40.31–40.26 (Ma) MECO-related cooling Regime III	40.26–40.21 (Ma) MECO cooling and TOC-rich Regime IV	40.21–39.80 (Ma) Post-MECO background Regime V	Average upper crust abundance[1]	Post-Archean average Australian shale[2]	Average shale[3]
Al (%)	2.8	3.2	3.2	4.8	3.0	8.0	8.4	8.9
Ba (ppm)	324	334	333	433	289	550	650	650
Cd (ppm)	2.5	3.3	2.9	6.0	2.9	0.1	0.1	0.3
Co (ppm)	5.8	6.1	5.8	7.5	5.6	17.0	20.0	19.0
Cr (ppm)	59	71	80	112	59	83	100	90
Cu (ppm)	44	38	44	77	56	25	75	45
Mn (ppm)	86	82	80	89	92	600	1400	850
Mo (ppm)	34.2	26.3	32.9	69.2	37.0	1.5	1.0	1.3
Ni (ppm)	62	61	68	112	65	44	60	68
V (ppm)	496	483	469	774	413	107	140	130
Zn (ppm)	87	93	84	140	78	71	80	95
Mn/Al	30	26	25	19	31	75	167	96
Ba/Al	114	105	105	90	96	68	77	73
Cd/Al	0.9	1.0	0.9	1.2	1.0	0.0	0.0	0.0
Co/Al	2.0	1.9	1.8	1.6	1.9	2.1	2.4	2.1
Cr/Al	21	22	25	23	20	10	12	10
Cu/Al	15.5	12.1	13.8	16.0	18.7	3.1	8.9	5.1
Mo/Al	12.0	8.3	10.3	14.4	12.3	0.2	0.1	0.1
Ni/Al	21.7	19.3	21.4	23.4	21.5	5.5	7.1	7.6
V/Al	174	153	147	161	137	13	17	15
Zn/Al	30.5	29.5	26.5	29.2	25.8	8.8	9.5	10.7

Note: The leftmost five columns give average values over regimes I–V of this study of the middle Eocene Belaya River section. The rightmost three columns give average values for the upper crust, post-Archean Australian shale, and average shale, from their respective references as compiled in Tribovillard et al. (2006): 1—McLennan (2001); 2—Taylor and McLennan (1985); 3—Wedepohl (1971, 1991). Cells are shaded per row (variable), with a darker gray representing a higher cell value. MECO—middle Eocene climatic optimum; TOC—total organic carbon.

oric water (e.g., Gat, 1996), but we consider trends and variability to reflect a primary signal, modulated by changes in lithology. Values decrease from –3.3‰ to –4.0‰ in regime III, followed by a transient shift to very low values of ~–5.5‰ at ca. 40.25 Ma (regime IV). The $\delta^{18}O_{carb}$ values subsequently return to –4.0‰ and gradually increase to –3.2‰ toward the top of the studied interval (regime V). By comparison, $\delta^{13}C_{carb}$ values vary from ~1.0‰ to ~1.5‰ in regimes I–III (Fig. 4E; Table 3), followed by a transient shift to ~2.0‰–2.5‰ in regime IV. The youngest interval (regime V) is characterized by a gradual increase from ~1.5‰ to ~2.0‰. The most prominent shifts, negative in $\delta^{18}O_{carb}$ and positive in $\delta^{13}C_{carb}$, occur in regime IV, synchronous with the $CaCO_3$ decrease, pointing to a link with this lithological change.

Organic Matter Composition

In regimes I and II, molar C_{org}/N_{tot} ratios are roughly ~15 to ~20 (Fig. 4G; Table 3). Subsequently, they gradually increase to values ranging between ~20 and ~25 in regime V. The largest increase in values occurs throughout regimes III and IV, with a sudden step in-between the regimes. Measured $\delta^{13}C_{org}$ varies around a value of –27.0‰ in regimes I–III (Fig. 4F; Table 3). Within regime IV, we observed a minor $\delta^{13}C_{org}$ decrease to –27.5‰, followed by a rapid increase to values of –26.5‰. In the youngest regime V, $\delta^{13}C_{org}$ values gradually return to –27.5‰. C_{org}/P_{tot} ratios are generally well above the Redfield ratio of 106 (Fig. 4H; Table 3). In regimes I–III, C_{org}/P_{tot} ratios are relatively stable, averaging ~160–200. At the start of regime IV, we recorded a rapid step in C_{org}/P_{tot} ratios from ~160 to ~270. Regime V retains higher values (~270) of C_{org}/P_{tot} compared to the older part of the record.

Trace Elements and Iron Speciation

Concentrations of Mo are well above the crustal average (1–2 ppm; Taylor and McLennan, 1985) for the entire record (Fig. 5D; Table 4). Concentrations average around 40 ppm at the base of the record, after which they decrease to more stable average values of ~30 ppm throughout regimes I–II. A distinct maximum in Mo with values up to 90 ppm is recorded in regime IV. In regime V, values stabilize to around ~40 ppm. Normalizing Mo to Al (Mo/Al) dampens the peak in regime IV but still reveals a similar trend of high values at the base of the record and in regime IV. Patterns of Mo/Al are generally mirrored by other redox-sensitive trace elements such as Ni and V (Fig. 5E; Table 4; Supplemental Material). Concentrations of Mn are stable and low (generally <100 ppm) for the entire record and always far below the crustal (600 ppm; McLennan, 2001) and shale (850 ppm; Wedepohl, 1971, 1991) averages. Al-normalized Mn values are higher at the base of the record and toward the top of the record (Fig. 5C; Table 4). Between 30% and 45% of the total Fe (Fe_{TOT}) in the studied record is highly reactive (Fe_{HR}), while between 50% and 90% of this Fe_{HR} is Fe in pyrite (Fig. 5F; Table 3). Broadly, Fe_{py}/Fe_{HR} ratios are high (>0.8) in organic-rich regime IV. Fe_{HR}/Fe_{TOT} ratios are slightly lower (~0.32) in regime III than in regime IV (~0.35) (Fig. 5G; Table 3).

Mercury Contents

Mercury (Hg) concentrations are between 10 and 50 ppb throughout the record (Fig. 5H; Table 3) and are strongly and significantly correlated to the C_{org} measured in the same samples. The Hg-C_{org} relationship is roughly linear, as often observed in modern sediments, all else being equal (Fig. S2; Percival et al., 2021, and references therein). The linear nature of the Hg-C_{org} relationship allows normalization of Hg to C_{org} to detect Hg-cycle perturbations (Sanei et al., 2012) (Fig. 5I; Table 3). Hg/C_{org} ratios are low on average (6–9 ppb/%), with a total range between 2 and 14 ppb/%. While the record shows variability, Hg/C_{org} values lack distinctive positive anomalies or a systematic change within the phase of gradual warming (regime II).

DISCUSSION

Depositional Setting and Source of Sedimentary Components

Sediments of the Kuma Formation at the Belaya River are characterized by relatively high C_{org} contents (background ~3%; this study; Sachsenhofer et al., 2018), similar to other studied localities on the Russian Platform and Scythian Platform (e.g., Gavrilov et al., 2000; Beniamovski et al., 2003), suggesting high productivity and/or preservation throughout the entire interval of Kuma Formation deposition. In the palynological residues, the organic matter consists of a mix of marine palynomorphs and large amounts of algal and (higher) plant-derived debris. While fairly

high ratios of C_{org}/N_{tot} (~20) might suggest pronounced contributions of terrestrial organic matter (Meyers, 1994), sedimentary C_{org}/N_{tot} values might also be elevated due to preferential loss of labile, nitrogen-rich components during early sedimentary diagenesis, as has been proposed for Cretaceous black shales (Junium and Arthur, 2007). Notably, there are no indications for high productivity in the dinocyst assemblage, as presumed heterotrophic peridinioid dinocysts are low in abundance. Taken together, high preservation is the most likely explanation for the high C_{org} observed here. BrGDGTs were below the detection limit in all samples, indicating a lack of erodible soils or soil mobilization in the hinterland, as well as low riverine and marine sedimentary brGDGT production and/or an enigmatic preferential transport process selecting against brGDGTs. The presence of brGMGTs despite the absence of brGDGTs suggests that these components were derived from a different source. Although a modern inventory of these components is required to fully assess their sourcing and proxy potential, H1020 was first identified in marine sediments (Liu et al., 2012) and was later shown to be abundant especially within the oxygen minimum zone of the marine water column (Xie et al., 2014). The latter study hypothesized anaerobic planktonic microbes as their main source, which might also be a possibility in our setting (see "Basin Restriction and Deoxygenation Associated with the Middle Eocene Climatic Optimum" in the "Discussion" section), analogous to the dominant marine source for brGMGT occurrences in Upper Paleocene and Lower Eocene sediments in the Arctic (Sluijs et al., 2020) and southwest Pacific Oceans (Bijl et al., 2021). In situ production in the sediments might be another possible source, as brGMGTs occur preferentially in the anoxic parts of lake sediments (Baxter et al., 2021).

High SSTs in the Middle Eocene Northern Peri-Tethys

We reconstructed tropically high SSTs in the Peri-Tethys throughout the middle Eocene, with background and peak SSTs of around 32 °C and 34 °C, respectively, when using an exponential (TEX_{86}^{H}; Kim et al., 2010) calibration, and 35 °C and 39 °C, respectively, when using a linear (Fig. 4; O'Brien et al., 2017) calibration. These temperatures are higher than coeval TEX_{86}-based temperatures from the equatorial and subtropical South Atlantic Ocean (Boscolo Galazzo et al., 2014; Cramwinckel et al., 2018). The first-order explanation for this difference is the context of the northern Peri-Tethys as an epicontinental or epeiric sea, a depositional environment that is typically a few degrees warmer than the mean ocean SST at the same latitude (e.g., Judd et al., 2020). It should be noted that, while our GDGT distributions point to marine Thaumarchaeotal production of the GDGTs comprising TEX_{86}, values of GDGT-2/GDGT-3 are high throughout and cross the suggested threshold of 5 (Taylor et al., 2013) in the lowermost and uppermost parts of the section. Above this threshold, TEX_{86} might additionally incorporate a signal that partially derives from deeper (>200 m) waters, possibly causing a bias in absolute reconstructed SST values. We, however, do not consider it likely that this affected our reconstructed temperature trends, as there are no large shifts in [2]/[3] ([2]/[3] values are <5 for most of the record), and there is no correlation between TEX_{86} and [2]/[3] (Supplemental Material). Reconstructed high temperatures might be supported by high fractional abundance of brGMGTs relative to brGDGTs (%brGMGT), which can be used as a temperature indicator in modern peats and lakes (Naafs et al., 2018; Baxter et al., 2019). This relationship has, however, not been constrained for marine environments, and, in our record, it is very much driven by total absence of brGDGTs. Within the brGMGT distributions, the fact that H1020 isomers are present, while H1034 and H1048 are absent, would likewise point to high temperatures, if the same relationship holds as in peats (Naafs et al., 2018).

Unexpectedly, the gradual warming that pinpoints the middle Eocene climatic optimum in the Belaya River section is not mirrored by gradual changes in the other analyzed sedimentary properties, such as lithology and redox-sensitive trace elements. This indicates that regionally in the Peri-Tethys, middle Eocene climatic optimum warming was not linked to strong changes in ocean chemistry or ecosystems. Because very strong deoxygenation and ecosystem change characterize Paleocene-Eocene thermal maximum warming in this region (Dickson et al., 2014; Shcherbinina et al., 2016), we surmise that the lower rate and/or amplitude of warming during the middle Eocene climatic optimum was insufficient to result in similar regional effects. Based on global compilations of records, middle Eocene climatic optimum warming seems to have been slightly smaller in amplitude than that during the Paleocene-Eocene thermal maximum (Dunkley Jones et al., 2013; Frieling et al., 2017). More notably, the much longer duration of the middle Eocene climatic optimum warming trend (several hundreds of thousands of years) implies that the average rate of warming was one or two orders of magnitude lower (e.g., Zeebe et al., 2016).

Regional Arc Volcanism as a Driver of Middle Eocene Climatic Optimum Warming

Our Hg/C_{org} record from the Kuma Formation does not contain major spikes that anomalously stand out from the bulk of the values (Fig. 5I; Fig. S3). Combined Hg and C_{org} values of the Belaya River section overlap with those of other sections that are characterized by relatively stable and high (>2%) C_{org}, but that are not marked by large igneous province volcanism (e.g., Grasby et al., 2019), such as the Jurassic Kimmeridge Clay (Percival et al., 2015) and sediments from the past ~160 k.y. in the Peruvian margin upwelling zone (Fig. S2; Shen et al., 2020). Despite a suggestive temporal correlation between middle Eocene climatic optimum warming and a continental arc flare-up related to Arabia-Eurasia collision (van der Boon et al., 2021), our Hg record does not show evidence for the increased local or regional volcanism that has been hypothesized to have contributed to a carbon cycle imbalance on the order of 2000–4000 Pg C (Kargaranbafghi and Neubauer, 2018; van der Boon et al., 2021).

The Belaya River is relatively close to the region of proposed volcanism, which would promote the use of the Hg proxy in this way. On the other hand, it is not clear whether the scale of the arc flare-up perturbation to the Hg cycle would have been sufficient to register in the Hg sedimentary record. Hg contents have, over recent years, been regularly applied to track large igneous province activity in the geologic record (e.g., Sanei et al., 2012; Percival et al., 2017; Jones et al., 2019). While Hg emissions from arc volcanism are certainly significant, it should be noted that a continental arc flare-up might result in different local and global Hg signatures compared to large igneous provinces. Sedimentary Hg records spanning periods with fluctuating or elevated volcanism, but not related to large igneous provinces, are very limited in number (e.g., Roos-Barraclough et al., 2002). A recent data compilation of Hg emissions encompassing active volcanoes suggests that arc volcanoes emit more Hg per year than non-arc volcanoes (Edwards et al., 2021). However, as Hg emitted per volume of volcanic gas is indistinguishable, this mainly results from the higher overall fluxes from studied arc volcanoes (Edwards et al., 2021). Long-term mean lava discharge rates over the approximately million-year lifetimes of some studied large igneous provinces are comparable to the long-term global mean arc magma discharge rate (Mather and Schmidt, 2021), suggesting that large igneous provinces likely represent a more significant perturbation to the Hg cycle than a

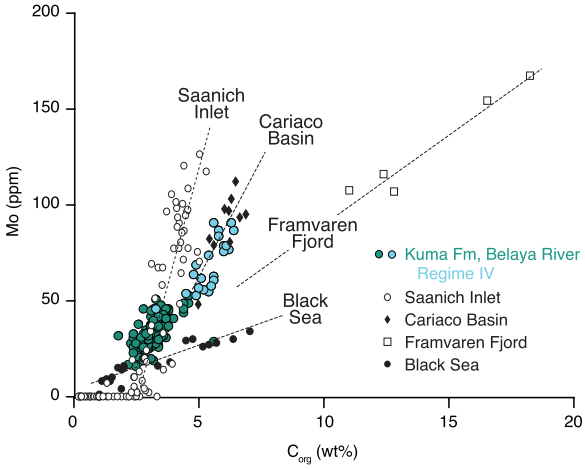

Figure 6. Relationship between molybdenum (Mo) vs. C_{org} for the Kuma Formation, Belaya River section. Cross-plot shows Mo contents (ppm) on the vertical axis against C_{org} contents (wt%) on the horizontal axis for the Kuma Formation, Belaya River section (dark gray dots; this study), with regime IV plotted separately (light gray dots), shown against modern marine data and their regression slopes from the weakly restricted Saanich Inlet to the severely restricted Black Sea (Algeo and Lyons, 2006).

single regional arc flare-up. Inferring eruption activity in volcanic arcs is further complicated by the observations from ice cores, which show far-field Hg spikes are not necessarily scaled to the volume of individual eruptions, likely as a result of heterogeneous dispersal and initial Hg loading (Schuster et al., 2002).

As poorly constrained as the mechanisms governing Hg emissions from volcanoes are, if we assume the 2000–4000 Pg C perturbation was entirely released from volcanism, with a Hg/CO_2 mass ratio of 10^{-8} to 10^{-6} (Witt et al., 2008), this would suggest associated Hg emissions in the range of 10^{11} to 10^{13} g. Even at the top of this range, this is significantly lower than estimates of Hg emissions from the Karoo-Ferrar large igneous province, on of order 10^{14} g (Percival et al., 2015), and would represent a reduced impact on the Hg cycle, and smaller likelihood of recording the perturbation, particularly given the shorter duration of the middle Eocene climatic optimum compared to a large igneous province event. Further work is required to understand whether Hg might be useful for constraining rates of non–large igneous province volcanism in the geologic record. Regarding the middle Eocene climatic optimum (and potentially similar warming events of similar duration and amplitude), we conclude that while an imbalance between volcanism and silicate weathering remains the most likely cause (e.g., van der Ploeg et al., 2018), pinpointing any exact regions of excess volcanic emissions remains challenging.

Basin Restriction and Deoxygenation Associated with the Middle Eocene Climatic Optimum

The largest changes in sediment composition ($CaCO_3$ decrease and C_{org} increase), the concomitant shifts in $\delta^{18}O_{carb}$ and $\delta^{13}C_{carb}$, and the most prominent changes in redox-sensitive proxies all occur during the second half of middle Eocene climatic optimum cooling, in regime IV (Tables 3 and 4; Figs. 4 and 5). The increased sedimentary C_{org} content in this interval may relate to high marine primary productivity and/or high preservation, the latter of which may have been affected by factors such as bottom-water deoxygenation and sedimentation rate (e.g., Berner and Raiswell, 1983; Middelburg and Levin, 2009). According to our age model, sediment accumulation rates increased from the middle Eocene climatic optimum onward from ~10 to ~45 m/m.y. (Fig. 3), likely facilitating enhanced C_{org} preservation (Canfield, 1994; Algeo et al., 2013; Schoepfer et al., 2015). Moreover, the concentrations of redox-sensitive elements and Fe-speciation data indicate variable levels of oxygenation throughout the studied section (Fig. 5; Table 4). As brGMGTs might be produced by anaerobic planktonic microbes (Xie et al., 2014), their high abundance relative to brGDGTs might also be related to low-oxygen conditions. C_{org}/P_{tot} ratios average 221, i.e., significantly above the Redfield ratio of 106 (Fig. 4), indicating preferential regeneration of P from the sediments under anoxic bottom waters (Algeo and Ingall, 2007). Besides C_{org} and C_{org}/P_{tot} ratios, some sedimentary (trace) metal concentrations are sensitive to bottom-water redox conditions (e.g., Calvert and Pedersen, 1993; Tribovillard et al., 2006; van Helmond et al., 2018). In particular, sedimentary Mo has been shown to be an accurate, semiquantitative redox proxy, as sedimentary enrichment of Mo increases when sulfide concentrations in pore waters and eventually bottom waters increase (e.g., Helz et al., 1996; Algeo and Tribovillard, 2009). The high Mo concentrations recorded in the Belaya River section (Fig. 5; Table 4) are indicative of intermittently euxinic bottom waters (i.e., free sulfide in the water column) and perhaps even (more) permanently euxinic bottom waters during phases of maximum enrichment, based on comparison with the distribution of sedimentary Mo in modern sulfidic marine systems (Fig. 6; Scott and Lyons, 2012). In contrast to Mo, Mn is mobilized under reducing conditions; i.e., sediments deposited under anoxic conditions are depleted in Mn (e.g., Thomson et al., 1995; van Helmond et al., 2014). This is also the case for the entire Belaya River record (Fig. 5; Table 4), supportive of deoxygenated bottom waters. This is furthermore in agreement with the observation that benthic foraminifera are absent throughout and in the middle-upper part of the Kuma Formation at the Belaya River (Popov et al., 2019b) and Kheu River sections (Beniamovski et al., 2003), respectively, suggesting anoxic conditions.

We used the speciation of Fe between different mineral phases to further investigate the degree of deoxygenation throughout the record. Under reducing conditions, a larger fraction of the total sedimentary Fe pool is highly reactive, thus leading to higher Fe_{HR}/Fe_{TOT} ratios. Based on values in both modern and ancient sediments, a Fe_{HR}/Fe_{TOT} ratio of 0.38 was found to separate oxic-suboxic conditions from anoxic-euxinic conditions (Poulton and Canfield, 2011), although verification with other proxies is recommended (Raiswell et al., 2018, and references therein). In the studied interval, Fe_{HR}/Fe_{TOT} are close to 0.38 for the entire record (Fig. 5F), consistent with the previously discussed proxies indicating alternating to persistent reducing conditions. Intensification of reducing conditions during middle Eocene climatic optimum cooling (regime IV) is highlighted by increases in redox-sensitive trace elements such as Mo and Ni, both in their concentrations in parts per million and when normalized to Al (Fig. 5; Table 4). In addition to Fe_{HR}/Fe_{TOT} ratios, the degree of Fe pyritization, as expressed in the Fe_{py}/Fe_{HR} ratio, can be used to reconstruct bottom-water redox conditions. In regime IV, this ratio exceeds 0.8 (Fig. 5G), indicating euxinic conditions were likely prevalent in the bottom waters (Anderson and Raiswell, 2004). Increased preservation of organic matter under low-oxygen conditions thus likely facilitated the sharp increase in C_{org} that is recorded in the section, in addition to the high sedimentation rates previously mentioned.

As this interval of intensified deoxygenation occurred during cooling following regional peak middle Eocene climatic optimum warmth, euxinia in the northern Peri-Tethys was not directly caused by ocean warming or associated sea-level rise. Interestingly, the slope of the Mo-C_{org} relationship decreases during

regime IV (Fig. 6). While most of the Belaya River samples fall on the regression line of the modern Saanich Inlet, the data from the C_{org}-rich interval overlap with the (more restricted) Cariaco Basin. This change could relate to reduced availability of aqueous Mo due to increased hydrographic restriction of the deep waters (Algeo and Lyons, 2006), pointing to a transient increase in basin restriction as a possible cause for the transient changes in oxygenation and sedimentary chemistry during middle Eocene climatic optimum cooling. Part of the sharp decline in $\delta^{18}O_{carb}$ in regime IV, coincident with Mo/C_{org}-based restriction, might therefore be explained by reduced surface-water $\delta^{18}O$, i.e., reduced salinity, caused by enhanced relative influence of freshwater input over marine connections. The interval of euxinia might therefore not have been directly tied to middle Eocene climatic optimum climate change; instead, it was likely a consequence of intensified ongoing tectonic restriction of the Peri-Tethys (Palcu and Krijgsman, 2022). Specifically, the intensified arc volcanism in the Iran-Anatolian region around middle Eocene climatic optimum times (Verdel et al., 2011; van der Boon et al., 2021) might well represent a step change in restriction of the southern gateways connecting the Peri-Tethys to the Indian Ocean (Palcu and Krijgsman, 2022), as regional mountain belts were uplifted (Keskin et al., 2008). The Peri-Tethys–Siberian (Turgay strait) and Siberian–Arctic (Kara strait) connections likewise show increased restriction around middle Eocene climatic optimum times (Palcu and Krijgsman, 2022). Interestingly, a shift to more arid conditions is recorded in dust records from central China at 40 Ma (Bosboom et al., 2014; Meijer et al., 2021), i.e., coincident with the middle Eocene climatic optimum, which Meijer et al. (2021) related to a major Peri-Tethys regression from the Tarim and Tajik basins around 41–40 Ma (Kaya et al., 2019). We surmise that increased restriction and euxinia in the Kuma basin can be mechanistically related to the observed middle Eocene climatic optimum–associated cooling if boreal surface inflow, e.g., from the North Sea, became dominant over the southern gateways, thereby suppressing middle Eocene climatic optimum warmth (Palcu and Krijgsman, 2022). Model simulations with sophisticated oceanography and bathymetry would be necessary to assess scenarios restricting different tropical and boreal gateways in the middle Eocene and their effects on Peri-Tethys SSTs and oxygenation. Nevertheless, this study highlights the importance of the interplay between global climate and regional gateway evolution in determining local climate and oceanographic change.

Quantification of Regional Excess Organic Carbon Burial and its Potential Role in Middle Eocene Climatic Optimum Recovery

According to our age constraints, sedimentation rates at the Belaya River section increased almost fivefold during the middle Eocene climatic optimum, while C_{org} contents during middle Eocene climatic optimum cooling (regime IV) record an increase from ~3 wt% to ~5.5 wt% over an interval of ~55 k.y. (Fig. 4). Using an estimated dry bulk sediment density of 2.5 g cm^{-3} together with the above values results in C_{org} mass accumulation rates of ~0.6 g C cm^{-2} $k.y.^{-1}$ for this interval. The Eocene Peri-Tethys was prone to developing (intensified) low-oxygen conditions, as evidenced both by the high organic content of the Kuma Formation in general (Beniamovski et al., 2003) and also by a similar deoxygenation response to Paleocene-Eocene thermal maximum warming ca. 56 Ma (Dickson et al., 2014) and potentially during later hyperthermal events (Radionova et al., 2003), and during the Eocene-Oligocene transition (Sachsenhofer et al., 2017). In order to provide a ballpark figure of total C_{org} burial in the northern Peri-Tethys during middle Eocene climatic optimum cooling, we estimated the areal extent of the Kuma Formation to be ~1.5×10^6 km^2, based on the area maps of Sachsenhofer et al. (2018). This is a conservative estimate, as organic-rich lateral equivalents of the Kuma Formation might extend further, such as past the Black Sea to the west (Hnylko and Hnylko, 2019). Using our values at the Belaya River section, we extrapolated the total C_{org} burial during middle Eocene climatic optimum cooling in the northern Peri-Tethys to be ~9.2 Tg C yr^{-1}, ~3% of the modern global C_{org} burial of ~300 Tg C yr^{-1} (Supplemental Material). This results in ~500 Pg buried C total over the whole 55 k.y. interval. Expressing this as excess burial relative to pre–middle Eocene climatic optimum values, and extrapolating from the Belaya River C_{org} and sedimentation rates, yields excess C_{org} burial of ~8.1 Tg C yr^{-1} and a total of ~450 Pg excess C_{org} buried. Such an amount might have played a significant role in middle Eocene climatic optimum CO_2 drawdown, but it was likely not of sufficient magnitude to explain the full recovery to a pre-event background global climate state. Yet, there are indications that middle Eocene climatic optimum–associated enhanced C_{org} burial might not have been limited to the Peri-Tethys region. A similar pattern of middle Eocene climatic optimum warming followed by enhanced sedimentary C_{org} content has been observed in sediments from the Alano di Piave section in Italy, central western Tethys (Fig. 1; Spofforth et al., 2010). At Alano, two $\delta^{13}C$-enriched, C_{org}-rich (~2 wt%) layers with a thickness of several meters occur in the post–middle Eocene climatic optimum interval. These layers are concurrent with planktic and benthic foraminiferal assemblages suggesting eutrophic sea-surface conditions, high export productivity, and oxygen-depleted bottom waters right after the zenith of middle Eocene climatic optimum warmth (Luciani et al., 2010; Boscolo Galazzo et al., 2013). This suggests that eutrophic and anoxic conditions facilitated production, preservation, and ultimately burial of C_{org}. The Monte Cagnero section in Italy records a similar $\delta^{13}C$-enriched post–middle Eocene climatic optimum layer with increased magnetic susceptibility, possibly likewise indicating C_{org} enrichment (Savian et al., 2014; Kochhann et al., 2021). The middle Eocene climatic optimum has also been recognized in other Tethyan sites, such as the Contessa Highway section, Italy (Jovane et al., 2007), the Elazig Basin, Turkey (Rodelli et al., 2017; Rego et al., 2018; Giorgioni et al., 2019), and the oil shales of Jordan (Hussein et al., 2014), but well-constrained C_{org} accumulation rates from multiple sites within and outside of the Tethys Ocean are lacking. For the present study, we therefore refrained from extrapolating C_{org} burial to outside of the Peri-Tethyan Kuma Formation. Still, we note that a subtle positive $\delta^{13}C$ trend and maximum after the peak $\delta^{18}O$ minimum in the global benthic stable isotope compilation (Bohaty et al., 2009; Westerhold et al., 2020) are consistent with a role for sequestration of relatively ^{12}C-rich C_{org} from the exogenic carbon pool, resulting in atmospheric CO_2 drawdown and climatic recovery following the middle Eocene climatic optimum. Estimating the amount of global C_{org} burial during middle Eocene climatic optimum recovery and modeling its consequences for climate and carbon cycling represent promising targets for future studies in order to improve our understanding of climate-carbon feedbacks during events on similar timescales to the middle Eocene climatic optimum.

CONCLUSION

The middle Eocene climatic optimum (ca. 40 Ma) was a period of transient global warming lasting ~400 k.y. that interrupted long-term Eocene cooling. The controls on its initiation and termination are poorly understood but might offer key insights into Earth's Eocene climate system. In this study, we targeted the organic-rich middle Eocene Kuma Formation in the Belaya River section, North Caucasus, in order to investigate the Peri-Tethyan response to the climatic changes of the middle Eocene climatic optimum in terms of regional temperature,

depositional environment, and carbon drawdown. We found that the middle Eocene Peri-Tethys was characterized by high TEX_{86}-based SSTs, on which middle Eocene climatic optimum warming stands out as an additional 2–3 °C rise (Fig. 4). A nearby contemporaneous arc-volcanism flare-up, evidenced by deposits left in modern-day Iran and hypothesized to play a role in driving environmental changes across the middle Eocene climatic optimum, left no clear trace in the sedimentary Hg record in the Belaya River section. However, it is currently uncertain whether volcanism on this scale is expected to perturb the global Hg cycle sufficiently to be recorded in the geologic record. Intriguingly, we found that the most striking changes in sediment lithology and geochemistry did not occur during middle Eocene climatic optimum warming or peak warmth, but were concomitant with subsequent cooling. Based on sedimentary trace-element compositions and iron speciation (Fig. 5), middle Eocene bottom waters in the study area were consistently reducing, with an alternation of suboxic, anoxic, and euxinic conditions. The most reducing conditions, with presumably euxinic bottom waters, occurred during the middle Eocene climatic optimum cooling phase, which was furthermore characterized by enhanced C_{org} burial. Extrapolating from our record, excess C_{org} burial might have been ~8.1 Tg C yr^{-1}, resulting in a total ~450 Pg of excess C_{org} buried over middle Eocene climatic optimum cooling in the northern Peri-Tethys. As indications for enhanced C_{org} burial also exist in the western Tethys, this phenomenon might have played a quantitatively significant role in middle Eocene climatic optimum recovery. This illustrates that the closing Tethys Ocean might have affected global Paleogene climate by functioning as a large organic carbon sink.

ACKNOWLEDGMENTS

This work was carried out under the program of the Netherlands Earth System Science Centre (NESSC), financially supported by the Dutch Ministry of Education, Culture and Science. We thank Sergey Popov and Larisa Golovina (Russian Academy of Sciences), Michael Morton and Sarah Davies (University of Leicester), Arjen Grothe and Kevin Vis (Utrecht University), and Stephen Vincent (Cambridge Arctic Shelf Programme, CASP, University of Cambridge) for field support and discussions. We thank Kirsten de Haan, Arnold van Dijk, Coen Mulder, and Natasja Welters (Utrecht University) for analytical support. T.A. Mather and J. Frieling acknowledge funding from a European Research Council (ERC) consolidator grant (ERC-2018-COG-818717-V-ECHO), A. Sluijs acknowledges ERC consolidator grant 771497 (SPANC), and C.P. Slomp and N.A.G.M. van Helmond acknowledge funding from Dutch Research Council (NWO) Vici grant 865.13.005. M.J. Cramwinckel and A. Sluijs thank the Ammodo Foundation for funding unfettered research by laureate A. Sluijs.

REFERENCES CITED

Agnini, C., Fornaciari, E., Giusberti, L., Grandesso, P., Lanci, L., Luciani, V., Muttoni, G., Pälike, H., Rio, D., Spofforth, D.J.A., and Stefani, C., 2011, Integrated biomagnetostratigraphy of the Alano section (NE Italy): A proposal for defining the middle-late Eocene boundary: Geological Society of America Bulletin, v. 123, p. 841–872, https://doi.org/10.1130/B30158.1.

Algeo, T.J., and Ingall, E., 2007, Sedimentary C_{org}:P ratios, paleocean ventilation, and Phanerozoic atmospheric pO_2: Palaeogeography, Palaeoclimatology, Palaeoecology, v. 256, p. 130–155, https://doi.org/10.1016/j.palaeo.2007.02.029.

Algeo, T.J., and Lyons, T.W., 2006, Mo–total organic carbon covariation in modern anoxic marine environments: Implications for analysis of paleoredox and paleohydrographic conditions: Paleoceanography, v. 21, PA1016, https://doi.org/10.1029/2004PA001112.

Algeo, T.J., and Tribovillard, N., 2009, Environmental analysis of paleoceanographic systems based on molybdenum-uranium covariation: Chemical Geology, v. 268, p. 211–225, https://doi.org/10.1016/j.chemgeo.2009.09.001.

Algeo, T.J., Henderson, C.M., Tong, J., Feng, Q., Yin, H., and Tyson, R.V., 2013, Plankton and productivity during the Permian-Triassic boundary crisis: An analysis of organic carbon fluxes: Global and Planetary Change, v. 105, p. 52–67, https://doi.org/10.1016/j.gloplacha.2012.02.008.

Allen, M.B., and Armstrong, H.A., 2008, Arabia-Eurasia collision and the forcing of mid-Cenozoic global cooling: Palaeogeography, Palaeoclimatology, Palaeoecology, v. 265, p. 52–58, https://doi.org/10.1016/j.palaeo.2008.04.021.

Anderson, T.F., and Raiswell, R., 2004, Sources and mechanisms for the enrichment of highly reactive iron in euxinic Black Sea sediments: American Journal of Science, v. 304, p. 203–233, https://doi.org/10.2475/ajs.304.3.203.

Arimoto, J., Nishi, H., Kuroyanagi, A., Takashima, R., Matsui, H., and Ikehara, M., 2020, Changes in upper ocean hydrography and productivity across the middle Eocene climatic optimum: Local insights and global implications from the Northwest Atlantic: Global and Planetary Change, v. 193, https://doi.org/10.1016/j.gloplacha.2020.103258.

Backman, J., and Shackleton, N.J., 1983, Quantitative biochronology of Pliocene and early Pleistocene calcareous nannofossils from the Atlantic, Indian and Pacific Oceans: Marine Micropaleontology, v. 8, p. 141–170, https://doi.org/10.1016/0377-8398(83)90009-9.

Bailey, D.K., 1992, Episodic alkaline igneous activity across Africa: Implications for the causes of continental breakup, *in* Storey, B.C., Alabaster, T., and Pankhurst, R.J., eds., Magmatism and the Causes of Continental Break-Up: Geological Society, London, Special Publication 68, p. 91–98, https://doi.org/10.1144/GSL.SP.1992.068.01.06.

Baxter, A.J., Hopmans, E.C., Russell, J.M., and Sinninghe Damsté, J.S., 2019, Bacterial GMGTs in East African lake sediments: Their potential as palaeotemperature indicators: Geochimica et Cosmochimica Acta, v. 259, p. 155–169, https://doi.org/10.1016/j.gca.2019.05.039.

Baxter, A.J., Peterse, F., Verschuren, D., and Sinninghe Damsté, J.S., 2021, Anoxic in situ production of bacterial GMGTs in the water column and surficial bottom sediments of a meromictic tropical crater lake: Implications for lake paleothermometry: Geochimica et Cosmochimica Acta, v. 306, p. 171–188, https://doi.org/10.1016/j.gca.2021.05.015.

Beniamovski, V.N., 2012, A high resolution Lutetian–Bartonian planktonic foraminiferal zonation in the Crimean-Caucasus region of the northeastern Peri-Tethys: Australian Journal of Earth Sciences, v. 105, p. 117–128.

Beniamovski, V.N., Alekseev, A.S., Ovechkina, M.N., and Oberhaensli, H., 2003, Middle to Upper Eocene dysoxic-anoxic Kuma Formation (northeast Peri-Tethys): Biostratigraphy and paleoenvironments, *in* Wing, S.L., Gingerich, P.D., Schmitz, B., and Thomas, E., eds., Causes and Consequences of Globally Warm Climates in the Early Paleogene: Geological Society of America Special Paper 369, p. 95–112, https://doi.org/10.1130/0-8137-2369-8.95.

Berner, R.A., and Raiswell, R., 1983, Burial of organic carbon and pyrite sulfur in sediments over Phanerozoic time: A new theory: Geochimica et Cosmochimica Acta, v. 47, p. 855–862, https://doi.org/10.1016/0016-7037(83)90151-5.

Bijl, P.K., Houben, A.J.P., Schouten, S., Bohaty, S.M., Sluijs, A., Reichart, G.-J., Damsté, J.S.S., and Brinkhuis, H., 2010, Transient middle Eocene atmospheric CO_2 and temperature variations: Science, v. 330, p. 819–821, https://doi.org/10.1126/science.1193654.

Bijl, P.K., Brinkhuis, H., Egger, L.M., Eldrett, J.S., Frieling, J., Grothe, A., Houben, A.J.P., Pross, J., Śliwińska, K.K., and Sluijs, A., 2017, Comment on "Wetzeliella and its allies—The 'hole' story: A taxonomic revision of the Paleogene dinoflagellate subfamily Wetzelielloideae" by Williams et al. (2015): Palynology, v. 41, p. 423–429, https://doi.org/10.1080/01916122.2016.1235056.

Bijl, P.K., Frieling, J., Cramwinckel, M.J., Boschman, C., Sluijs, A., and Peterse, F., 2021, Maastrichtian–Rupelian paleoclimates in the southwest Pacific—A critical re-evaluation of biomarker paleothermometry and dinoflagellate cyst paleoecology at Ocean Drilling Program Site 1172: Climate of the Past, v. 17, p. 2393–2425, https://doi.org/10.5194/cp-17-2393-2021.

Blaga, C.I., Reichart, G.-J., Heiri, O., and Damsté, J.S.S., 2009, Tetraether membrane lipid distributions in water-column particulate matter and sediments: A study of 47 European lakes along a north-south transect: Journal of Paleolimnology, v. 41, p. 523–540, https://doi.org/10.1007/s10933-008-9242-2.

Bohaty, S.M., and Zachos, J.C., 2003, Significant Southern Ocean warming event in the late middle Eocene: Geology, v. 31, p. 1017–1020, https://doi.org/10.1130/G19800.1.

Bohaty, S.M., Zachos, J.C., Florindo, F., and Delaney, M.L., 2009, Coupled greenhouse warming and deep-sea acidification in the middle Eocene: Paleoceanography, v. 24, PA2207, https://doi.org/10.1029/2008PA001676.

Bosboom, R.E., Abels, H.A., Hoorn, C., van den Berg, B.C.J., Guo, Z., and Dupont-Nivet, G., 2014, Aridification in continental Asia after the middle Eocene climatic optimum (MECO): Earth and Planetary Science Letters, v. 389, p. 34–42, https://doi.org/10.1016/j.epsl.2013.12.014.

Boscolo Galazzo, F., Giusberti, L., Luciani, V., and Thomas, E., 2013, Paleoenvironmental changes during the middle Eocene climatic optimum (MECO) and its aftermath: The benthic foraminiferal record from the Alano section (NE Italy): Palaeogeography, Palaeoclimatology, Palaeoecology, v. 378, p. 22–35, https://doi.org/10.1016/j.palaeo.2013.03.018.

Boscolo Galazzo, F., Thomas, E., Pagani, M., Warren, C., Luciani, V., and Giusberti, L., 2014, The middle Eocene climatic optimum (MECO): A multiproxy record of paleoceanographic changes in the southeast Atlantic (ODP Site 1263, Walvis Ridge): Paleoceanography, v. 29, p. 1143–1161, https://doi.org/10.1002/2014PA002670.

Bown, P.R., and Young, J.R., 1998, Techniques, *in* Bown, P.R., ed., Calcareous Nannofossil Biostratigraphy: London, Chapman and Hall/Kluwer Academic Publishers, p. 16–28.

Breitburg, D., Levin, L.A., Oschlies, A., Grégoire, M., Chavez, F.P., Conley, D.J., Garçon, V., Gilbert, D., Gutiérrez, D., Isensee, K., Jacinto, G.S., Limburg, K.E., Montes, I., Naqvi, S.W.A., Pitcher, G.C., Rabalais, N.N., Roman, M.R., Rose, K.A., Seibel, B.A., Telszewski, M., Yasuhara, M., and Zhang, J., 2018, Declining oxygen in the global ocean and coastal waters: Science, v. 359, https://doi.org/10.1126/science.aam7240.

Burke, K.D., Williams, J.W., Chandler, M.A., Haywood, A.M., Lunt, D.J., and Otto-Bliesner, B.L., 2018, Pliocene and Eocene provide best analogs for near-future climates: Proceedings of the National Academy of Sciences of the United States of America, v. 115, p. 13,288–13,293, https://doi.org/10.1073/pnas.1809600115.

Calvert, S.E., and Pedersen, T.F., 1993, Geochemistry of Recent oxic and anoxic marine sediments: Implications for the geological record: Marine Geology, v. 113, p. 67–88, https://doi.org/10.1016/0025-3227(93)90150-T.

Canfield, D.E., 1994, Factors influencing organic carbon preservation in marine sediments: Chemical Geology, v. 114, p. 315–329, https://doi.org/10.1016/0009-2541(94)90061-2.

Caves, J.K., Jost, A.B., Lau, K.V., and Maher, K., 2016, Cenozoic carbon cycle imbalances and a variable weathering feedback: Earth and Planetary Science Letters, v. 450, p. 152–163, https://doi.org/10.1016/j.epsl.2016.06.035.

Cramwinckel, M.J., Huber, M., Kocken, I.J., Agnini, C., Bijl, P.K., Bohaty, S.M., Frieling, J., Goldner, A., Hilgen, F.J., Kip, E.L., Peterse, F., van der Ploeg, R., Röhl, U., Schouten, S., and Sluijs, A., 2018, Synchronous tropical and polar temperature evolution in the Eocene: Nature, v. 559, p. 382–386, https://doi.org/10.1038/s41586-018-0272-2.

Cramwinckel, M.J., Coxall, H.K., Śliwińska, K.K., Polling, M., Harper, D.T., Bijl, P.K., Brinkhuis, H., Eldrett, J.S., Houben, A.J.P., Peterse, F., Schouten, S., Reichart, G.-J., Zachos, J.C., and Sluijs, A., 2020a, A warm, stratified, and restricted Labrador Sea across the middle Eocene and its climatic optimum: Paleoceanography and Paleoclimatology, v. 35, https://doi.org/10.1029/2020PA003932.

Cramwinckel, M.J., Woelders, L., Huurdeman, E.P., Peterse, F., Gallagher, S.J., Pross, J., Burgess, C.E., Reichart, G.-J., Sluijs, A., and Bijl, P.K., 2020b, Surface-circulation change in the southwest Pacific Ocean across the middle Eocene climatic optimum: Inferences from dinoflagellate cysts and biomarker paleothermometry: Climate of the Past, v. 16, p. 1667–1689, https://doi.org/10.5194/cp-16-1667-2020.

Dawber, C.F., and Tripati, A.K., 2011, Constraints on glaciation in the middle Eocene (46–37 Ma) from Ocean Drilling Program (ODP) Site 1209 in the tropical Pacific Ocean: Paleoceanography, v. 26, PA2208, https://doi.org/10.1029/2010PA002037.

Dickens, G.R., 2001, Carbon addition and removal during the late Palaeocene thermal maximum: Basic theory with a preliminary treatment of the isotope record at ODP Site 1051, Blake Nose, *in* Kroon, D., Norris, R.D., and Klaus, A., eds., Western North Atlantic Paleogene and Cretaceous Palaeoceanography: Geological Society, London, Special Publication 183, p. 293–305, https://doi.org/10.1144/GSL.SP.2001.183.01.14.

Dickson, A.J., Rees-Owen, R.L., März, C., Coe, A.L., Cohen, A.S., Pancost, R.D., Taylor, K., and Shcherbinina, E., 2014, The spread of marine anoxia on the northern Tethys margin during the Paleocene-Eocene thermal maximum: Paleoceanography, v. 29, p. 471–488, https://doi.org/10.1002/2014PA002629.

Doney, S.C., Fabry, V.J., Feely, R.A., and Kleypas, J.A., 2009, Ocean acidification: The other CO_2 problem: Annual Review of Marine Science, v. 1, p. 169–192, https://doi.org/10.1146/annurev.marine.010908.163834.

Dunkley Jones, T., Lunt, D.J., Schmidt, D.N., Ridgwell, A., Sluijs, A., Valdes, P.J., and Maslin, M., 2013, Climate model and proxy data constraints on ocean warming across the Paleocene-Eocene thermal maximum: Earth-Science Reviews, v. 125, p. 123–145, https://doi.org/10.1016/j.earscirev.2013.07.004.

Edgar, K.M., Wilson, P.A., Sexton, P.F., Gibbs, S.J., Roberts, A.P., and Norris, R.D., 2010, New biostratigraphic, magnetostratigraphic and isotopic insights into the middle Eocene climatic optimum in low latitudes: Palaeogeography, Palaeoclimatology, Palaeoecology, v. 297, p. 670–682, https://doi.org/10.1016/j.palaeo.2010.09.016.

Edgar, K.M., Bohaty, S.M., Coxall, H.K., Bown, P.R., Batenburg, S.J., Lear, C.H., and Pearson, P.N., 2020, New composite bio- and isotope stratigraphies spanning the middle Eocene climatic optimum at tropical ODP Site 865 in the Pacific Ocean: Journal of Micropalaeontology, v. 39, p. 117–138, https://doi.org/10.5194/jm-39-117-2020.

Edwards, B.A., Kushner, D.S., Outridge, P.M., and Wang, F., 2021, Fifty years of volcanic mercury emission research: Knowledge gaps and future directions: The Science of the Total Environment, v. 757, https://doi.org/10.1016/j.scitotenv.2020.143800.

Evans, D., Sagoo, N., Renema, W., Cotton, L.J., Müller, W., Todd, J.A., Saraswati, P.K., Stassen, P., Ziegler, M., Pearson, P.N., Valdes, P.J., and Affek, H.P., 2018, Eocene greenhouse climate revealed by coupled clumped isotope–Mg/Ca thermometry: Proceedings of the National Academy of Sciences of the United States of America, v. 115, p. 1174–1179, https://doi.org/10.1073/pnas.1714744115.

Frieling, J., and Sluijs, A., 2018, Towards quantitative environmental reconstructions from ancient non-analogue microfossil assemblages: Ecological preferences of Paleocene–Eocene dinoflagellates: Earth-Science Reviews, v. 185, p. 956–973, https://doi.org/10.1016/j.earscirev.2018.08.014.

Frieling, J., Gebhardt, H., Huber, M., Adekeye, O.A., Akande, S.O., Reichart, G.-J., Middelburg, J.J., Schouten, S., and Sluijs, A., 2017, Extreme warmth and heat-stressed plankton in the tropics during the Paleocene-Eocene thermal maximum: Science Advances, v. 3, https://doi.org/10.1126/sciadv.1600891.

Gat, J.R., 1996, Oxygen and hydrogen isotopes in the hydrologic cycle: Annual Review of Earth and Planetary Sciences, v. 24, p. 225–262, https://doi.org/10.1146/annurev.earth.24.1.225.

Gavrilov, Y.O., Shcherbinina, E.A., and Muzylöv, N.G., 2000, A Paleogene sequence in central North Caucasus: A response to paleoenvironmental changes: GFF, v. 122, p. 51–53, https://doi.org/10.1080/11035890001221051.

Giorgioni, M., Jovane, L., Rego, E.S., Rodelli, D., Frontalini, F., Coccioni, R., Catanzariti, R., and Özcan, E., 2019, Carbon cycle instability and orbital forcing during the middle Eocene climatic optimum: Scientific Reports, v. 9, p. 9357, https://doi.org/10.1038/s41598-019-45763-2.

Gradstein, F.M., Ogg, J.G., Schmitz, M.D., and Ogg, G.M., The Geologic Time Scale 2012: Amsterdam, Netherlands, Elsevier Science Limited, 1144 p.

Grasby, S.E., Them, T.R., Chen, Z., Yin, R., and Ardakani, O.H., 2019, Mercury as a proxy for volcanic emissions in the geologic record: Earth-Science Reviews, v. 196, https://doi.org/10.1016/j.earscirev.2019.102880.

Gruber, N., 2011, Warming up, turning sour, losing breath: Ocean biogeochemistry under global change: Philosophical Transactions of the Royal Society of London A: Mathematical, Physical and Engineering Sciences, v. 369, p. 1980–1996, https://doi.org/10.1098/rsta.2011.0003.

Helz, G.R., Miller, C.V., Charnock, J.M., Mosselmans, J.F.W., Pattrick, R.A.D., Garner, C.D., and Vaughan, D.J., 1996, Mechanism of molybdenum removal from the sea and its concentration in black shales: EXAFS evidence: Geochimica et Cosmochimica Acta, v. 60, p. 3631–3642, https://doi.org/10.1016/0016-7037(96)00195-0.

Henehan, M.J., Edgar, K.M., Foster, G.L., Penman, D.E., Hull, P.M., Greenop, R., Anagnostou, E., and Pearson, P.N., 2020, Revisiting the middle Eocene climatic optimum "carbon cycle conundrum" with new estimates of atmospheric pCO_2 from boron isotopes: Paleoceanography and Paleoclimatology, v. 35, https://doi.org/10.1029/2019PA003713.

Hnylko, O., and Hnylko, S., 2019, Geological environments forming the Eocene black-shale formation of the Silesian Nappe (Ukrainian Carpathians): Geodynamics, v. 26, no. 1, p. 60–75.

Hollis, C.J., Dunkley Jones, T., Anagnostou, E., Bijl, P.K., Cramwinckel, M.J., Cui, Y., Dickens, G.R., Edgar, K.M., Eley, Y., Evans, D., Foster, G.L., Frieling, J., Inglis, G.N., Kennedy, E.M., Kozdon, R., Lauretano, V., Lear, C.H., Littler, K., Lourens, L., Meckler, A.N., Naafs, B.D.A., Pälike, H., Pancost, R.D., Pearson, P.N., Röhl, U., Royer, D.L., Salzmann, U., Schubert, B.A., Seebeck, H., Sluijs, A., Speijer, R.P., Stassen, P., Tierney, J., Tripati, A., Wade, B., Westerhold, T., Witkowski, C., Zachos, J.C., Zhang, Y.G., Huber, M., and Lunt, D.J., 2019, The DeepMIP contribution to PMIP4: Methodologies for selection, compilation and analysis of latest Paleocene and early Eocene climate proxy data, incorporating version 0.1 of the DeepMIP database: Geoscientific Model Development, v. 12, p. 3149–3206, https://doi.org/10.5194/gmd-12-3149-2019.

Hopmans, E.C., Weijers, J.W.H., Schefuß, E., Herfort, L., Sinninghe Damsté, J.S., and Schouten, S., 2004, A novel proxy for terrestrial organic matter in sediments based on branched and isoprenoid tetraether lipids: Earth and Planetary Science Letters, v. 224, p. 107–116, https://doi.org/10.1016/j.epsl.2004.05.012.

Hopmans, E.C., Schouten, S., and Sinninghe Damsté, J.S., 2016, The effect of improved chromatography on GDGT-based palaeoproxies: Organic Geochemistry, v. 93, p. 1–6, https://doi.org/10.1016/j.orggeochem.2015.12.006.

Hussein, M.A., Alqudah, M., van den Boorn, S., Kolonic, S., Podlaha, O.G., and Mutterlose, J., 2014, Eocene oil shales from Jordan—Their petrography, carbon and oxygen stable isotopes: GeoArabia, v. 19, p. 139–162, https://doi.org/10.2113/geoarabia1903139.

Inglis, G.N., Farnsworth, A., Lunt, D., Foster, G.L., Hollis, C.J., Pagani, M., Jardine, P.E., Pearson, P.N., Markwick, P., Galsworthy, A.M.J., Raynham, L., Taylor, K.W.R., and Pancost, R.D., 2015, Descent toward the icehouse: Eocene sea surface cooling inferred from GDGT distributions: Paleoceanography, v. 30, https://doi.org/10.1002/2014PA002723.

Intergovernmental Panel on Climate Change (IPCC), 2019, IPCC Special Report on the Ocean and Cryosphere in a Changing Climate: Geneva, Switzerland, Intergovernmental Panel on Climate Change, 765 p.

Jones, M.T., Percival, L.M.E., Stokke, E.W., Frieling, J., Mather, T.A., Riber, L., Schubert, B.A., Schultz, B., Tegner, C., Planke, S., and Svensen, H.H., 2019, Mercury anomalies across the Palaeocene-Eocene thermal maximum: Climate of the Past, v. 15, p. 217–236, https://doi.org/10.5194/cp-15-217-2019.

Jovane, L., Florindo, F., Coccioni, R., Dinarès-Turell, J., Marsili, A., Monechi, S., Roberts, A.P., and Sprovieri, M., 2007, The middle Eocene climatic optimum event in the Contessa Highway section, Umbrian Apennines, Italy: Geological Society of America Bulletin, v. 119, p. 413–427, https://doi.org/10.1130/B25917.1.

Judd, E.J., Bhattacharya, T., and Ivany, L.C., 2020, A dynamical framework for interpreting ancient sea surface temperatures: Geophysical Research Letters, v. 47, https://doi.org/10.1029/2020GL089044.

Junium, C.K., and Arthur, M.A., 2007, Nitrogen cycling during the Cretaceous, Cenomanian–Turonian oceanic anoxic event II: Geochemistry Geophysics Geosystems, v. 8, Q03002, https://doi.org/10.1029/2006GC001328.

Kargaranbafghi, F., and Neubauer, F., 2018, Tectonic forcing to global cooling and aridification at the Eocene-Oligocene transition in the Iranian plateau: Global and Planetary Change, v. 171, p. 248–254, https://doi.org/10.1016/j.gloplacha.2017.12.012.

Kaya, M.Y., Dupont-Nivet, G., Proust, J.-N., Roperch, P., Bougeois, L., Meijer, N., Frieling, J., Fioroni, C., Altıner, S.Ö., Vardar, E., Barbolini, N., Stoica, M., Aminov, J., Mamtimin, M., and Zhaojie, G., 2019, Paleogene evolution and demise of the proto-Paratethys Sea in Central Asia (Tarim and Tajik basins): Role of intensified tectonic activity at ca. 41 Ma: Basin Research, v. 31, p. 461–486, https://doi.org/10.1111/bre.12330.

Kerrick, D.M., and Caldeira, K., 1999, Was the Himalayan orogen a climatically significant coupled source and sink for atmospheric CO_2 during the Cenozoic?: Earth and Planetary Science Letters, v. 173, p. 195–203, https://doi.org/10.1016/S0012-821X(99)00229-0.

Keskin, M., Genç, Ş.C., and Tüysüz, O., 2008, Petrology and geochemistry of post-collisional middle Eocene volcanic units in north-central Turkey: Evidence for magma generation by slab breakoff following the closure of the northern Neotethys Ocean: Lithos, v. 104, p. 267–305, https://doi.org/10.1016/j.lithos.2007.12.011.

Kim, J.-H., van der Meer, J., Schouten, S., Helmke, P., Willmott, V., Sangiorgi, F., Koç, N., Hopmans, E.C., and Damsté, J.S.S., 2010, New indices and calibrations derived from the distribution of crenarchaeal isoprenoid tetraether lipids: Implications for past sea surface temperature reconstructions: Geochimica et Cosmochimica Acta, v. 74, p. 4639–4654, https://doi.org/10.1016/j.gca.2010.05.027.

Kochhann, M.V.L., Savian, J.F., Tori, F., Catanzariti, R., Coccioni, R., Frontalini, F., Jovane, L., Florindo, F., and Monechi, S., 2021, Orbital tuning for the middle Eocene to early Oligocene Monte Cagnero section (central Italy): Paleoenvironmental and paleoclimatic implications: Palaeogeography, Palaeoclimatology, Palaeoecology, v. 577, https://doi.org/10.1016/j.palaeo.2021.110563.

Krasheninnikov, V.A., 1986, The Kuban River sequence (USSR, North Caucasus), *in* Pomerol, Ch., and Premoli-Silva, I., eds., Terminal Eocene Events: Amsterdam, Netherlands, Elsevier, Developments in Palaeontology and Stratigraphy 9, p. 137–139, https://doi.org/10.1016/S0920-5446(08)70109-2.

Kump, L.R., and Arthur, M.A., 1999, Interpreting carbon-isotope excursions: Carbonates and organic matter: Chemical Geology, v. 161, p. 181–198, https://doi.org/10.1016/S0009-2541(99)00086-8.

Liu, X.-L., Summons, R.E., and Hinrichs, K.-U., 2012, Extending the known range of glycerol ether lipids in the environment: Structural assignments based on tandem mass spectral fragmentation patterns: Rapid Communications in Mass Spectrometry, v. 26, p. 2295–2302, https://doi.org/10.1002/rcm.6355.

Luciani, V., Giusberti, L., Agnini, C., Fornaciari, E., Rio, D., Spofforth, D.J.A., and Pälike, H., 2010, Ecological and evolutionary response of Tethyan planktonic foraminifera to the middle Eocene climatic optimum (MECO) from the Alano section (NE Italy): Palaeogeography, Palaeoclimatology, Palaeoecology, v. 292, p. 82–95, https://doi.org/10.1016/j.palaeo.2010.03.029.

Mather, T.A., and Schmidt, A., 2021, Environmental effects of volcanic volatile fluxes from subaerial large igneous provinces, *in* Ernst, R.E., Dickson, A.J., and Bekker, A., eds., Large Igneous Provinces: A Driver of Global Environmental and Biotic Changes: American Geophysical Union Geophysical Monograph 255, p. 103–116, https://doi.org/10.1002/9781119507444.ch4.

Meijer, N., Dupont-Nivet, G., Barbolini, N., Woutersen, A., Rohrmann, A., Zhang, Y., Liu, X.-J., Licht, A., Abels, H.A., Hoorn, C., Tjallingii, R., Andermann, C., Dietze, M., and Nowaczyk, N., 2021, Loess-like dust appearance at 40 Ma in central China: Paleoceanography and Paleoclimatology, v. 36, https://doi.org/10.1029/2020PA003993.

Meyers, P., 1994, Preservation of elemental and isotopic source identification of sedimentary organic matter: Chemical Geology, v. 114, p. 289–302, https://doi.org/10.1016/0009-2541(94)90059-0.

Middelburg, J.J., and Levin, L.A., 2009, Coastal hypoxia and sediment biogeochemistry: Biogeosciences, v. 6, p. 1273–1293, https://doi.org/10.5194/bg-6-1273-2009.

Mjelde, R., Breivik, A.J., Raum, T., Mittelstaedt, E., Ito, G., and Faleide, J.I., 2008, Magmatic and tectonic evolution of the North Atlantic: Journal of the Geological Society, v. 165, p. 31–42, https://doi.org/10.1144/0016-76492007-018.

Morii, H., Eguchi, T., Nishihara, M., Kakinuma, K., König, H., and Koga, Y., 1998, A novel ether core lipid with H-shaped C80-isoprenoid hydrocarbon chain from the hyperthermophilic methanogen *Methanothermus fervidus*: Biochimica et Biophysica Acta (BBA)—Lipids and Lipid Metabolism, v. 1390, p. 339–345, https://doi.org/10.1016/S0005-2760(97)00183-5.

Naafs, B.D.A., McCormick, D., Inglis, G.N., and Pancost, R.D., 2018, Archaeal and bacterial H-GDGTs are abundant in peat and their relative abundance is positively correlated with temperature: Geochimica et Cosmochimica Acta, v. 227, p. 156–170, https://doi.org/10.1016/j.gca.2018.02.025.

O'Brien, C.L., Robinson, S.A., Pancost, R.D., Sinninghe Damsté, J.S., Schouten, S., Lunt, D.J., Alsenz, H., Bornemann, A., Bottini, C., Brassell, S.C., Farnsworth, A., Forster, A., Huber, B.T., Inglis, G.N., Jenkyns, H.C., Linnert, C., Littler, K., Markwick, P., McAnena, A., Mutterlose, J., Naafs, B.D.A., Püttmann, W., Sluijs, A., van Helmond, N.A.G.M., Vellekoop, J., Wagner, T., and Wrobel, N.E., 2017, Cretaceous sea-surface temperature evolution: Constraints from TEX86 and planktonic foraminiferal oxygen isotopes: Earth-Science Reviews, v. 172, p. 224–247, https://doi.org/10.1016/j.earscirev.2017.07.012.

Palcu, D.V., and Krijgsman, W., 2022, The dire straits of Paratethys: Gateways to the anoxic giant of Eurasia, *in* Srivastava, R.K., Ernst, R.E., Buchan, K.L., and de Kock, M., eds., Large Igneous Provinces and their Plumbing Systems: Geological Society, London, Special Publication 523 (in press), https://doi.org/10.1144/SP523-2021-73.

Papadomanolaki, N.M., Sluijs, A., and Slomp, C.P., 2022, Eutrophication and deoxygenation forcing of marginal marine organic carbon burial during the PETM: Paleoceanography and Paleoclimatology, v. 37, https://doi.org/10.1029/2021PA004232.

Percival, L.M.E., Witt, M.L.I., Mather, T.A., Hermoso, M., Jenkyns, H.C., Hesselbo, S.P., Al-Suwaidi, A.H., Storm, M.S., Xu, W., and Ruhl, M., 2015, Globally enhanced mercury deposition during the end-Pliensbachian extinction and Toarcian OAE: A link to the Karoo-Ferrar large igneous province: Earth and Planetary Science Letters, v. 428, p. 267–280, https://doi.org/10.1016/j.epsl.2015.06.064.

Percival, L.M.E., Ruhl, M., Hesselbo, S.P., Jenkyns, H.C., Mather, T.A., and Whiteside, J.H., 2017, Mercury evidence for pulsed volcanism during the end-Triassic mass extinction: Proceedings of the National Academy of Sciences of the United States of America, v. 114, p. 7929–7934, https://doi.org/10.1073/pnas.1705378114.

Percival, L.M.E., Bergquist, B.A., Mather, T.A., and Sanei, H., 2021, Sedimentary mercury enrichments as a tracer of large igneous province volcanism, *in* Ernst, R.E., Dickson, A.J., and Bekker, A., eds., Large Igneous Provinces: A Driver of Global Environmental and Biotic Changes: American Geophysical Union Geophysical Monograph 255, p. 247–262, https://doi.org/10.1002/9781119507444.ch11.

Pogge von Strandmann, P.A.E., Jones, M.T., West, A.J., Murphy, M.J., Stokke, E.W., Tarbuck, G., Wilson, D.J., Pearce, C.R., and Schmidt, D.N., 2021 Lithium isotope evidence for enhanced weathering and erosion during the Paleocene-Eocene thermal maximum: Science Advances, v. 7, https://doi.org/10.1126/sciadv.abh4224.

Popov, S.V., Tabachnikova, I.P., Bannikov, A.F., Sytchevskaya, E.K., Pinchuk, T.N., Akhmet'ev, M.A., Zaporozhets, N.I., van der Boon, A., Krijgsman, W., Stolyarov, A.S., and Krhovsky, J., 2019a, Lectostratotype of the Maikopian Group in the Belaya River section upstream of the town of Maikop (western Ciscaucasia) in the Oligocene part: Stratigraphy and Geological Correlation, v. 27, p. 339–360, https://doi.org/10.1134/S0869593819030043.

Popov, S.V., Tabachnikova, I.P., Pinchuk, T.N., Akhmetiev, M.A., and Zaporozhets, N.I., 2019b, The reference section of Eocene deposits in the Belaya River Valley, Adygea, western Ciscaucasia: Stratigraphy and Geological Correlation, v. 27, p. 118–132, https://doi.org/10.1134/S0869593819010052.

Poulton, S.W., and Canfield, D.E., 2011, Ferruginous conditions: A dominant feature of the ocean through Earth's history: Elements, v. 7, p. 107–112, https://doi.org/10.2113/gselements.7.2.107.

Pross, J., and Brinkhuis, H., 2005, Organic-walled dinoflagellate cysts as paleoenvironmental indicators in the Paleogene: A synopsis of concepts: Palaontologische Zeitschrift, v. 79, p. 53–59, https://doi.org/10.1007/BF03021753.

Radionova, E.P., Beniamovski, V.N., Iakovleva, A.I., Muzylöv, N.G., Oreshkina, T.V., Shcherbinina, E.A., and Kozlova, G.E., 2003, Early Paleogene transgressions: Stratigraphical and sedimentological evidence from the northern Peri-Tethys, *in* Wing, S.L., Gingerich, P.D., Schmitz, B., and Thomas, E., eds., Causes and Consequences of Globally Warm Climates in the Early Paleogene: Geological Society of America Special Paper 369, p. 239–261, https://doi.org/10.1130/0-8137-2369-8.239.

Raiswell, R., Hardisty, D.S., Lyons, T.W., Canfield, D.E., Owens, J.D., Planavsky, N.J., Poulton, S.W., and Reinhard, C.T., 2018, The iron paleoredox proxies: A guide to the pitfalls, problems and proper practice: American Journal of Science, v. 318, p. 491–526, https://doi.org/10.2475/05.2018.03.

Ravizza, G., Norris, R.N., Blusztajn, J., and Aubry, M.-P., 2001, An osmium isotope excursion associated with the late Paleocene thermal maximum: Evidence of intensified chemical weathering: Paleoceanography, v. 16, p. 155–163, https://doi.org/10.1029/2000PA000541.

Rego, E.S., Jovane, L., Hein, J.R., Sant'Anna, L.G., Giorgioni, M., Rodelli, D., and Özcan, E., 2018, Mineralogical evidence for warm and dry climatic conditions in the Neo-Tethys (eastern Turkey) during the middle Eocene: Palaeogeography, Palaeoclimatology, Palaeoecology, v. 501, p. 45–57, https://doi.org/10.1016/j.palaeo.2018.04.007.

Rodelli, D., Jovane, L., Özcan, E., Giorgioni, M., Coccioni, R., Frontalini, F., Rego, E.S., Brogi, A., Catanzariti, R., Less, G., and Rostami, M.A., 2017, High-resolution integrated magnetobiostratigraphy of a new middle Eocene section from the Neotethys (Elazığ Basin, eastern Turkey): Geological Society of America Bulletin, v. 130, p. 193–207, https://doi.org/10.1130/B31704.1.

Roos-Barraclough, F., Martinez-Cortizas, A., García-Rodeja, E., and Shotyk, W., 2002, A 14,500 year record of the accumulation of atmospheric mercury in peat: Volcanic signals, anthropogenic influences and a correlation to bromine accumulation: Earth and Planetary Science Letters, v. 202, p. 435–451, https://doi.org/10.1016/S0012-821X(02)00805-1.

Sachsenhofer, R.F., Popov, S.V., Akhmetiev, M.A., Bechtel, A., Gratzer, R., Groß, D., Horsfield, B., Rachetti, A., Rupprecht, B., Schaffar, W.B.H., and Zaporozhets, N.I., 2017, The type section of the Maikop Group (Oligocene–Lower Miocene) at the Belaya River (North Caucasus): Depositional environment and hydrocarbon potential: American Association of Petroleum Geologists Bulletin, v. 101, p. 289–319, https://doi.org/10.1306/08051616027.

Sachsenhofer, R.F., Popov, S.V., Coric, S., Mayer, J., Misch, D., Morton, M.T., Pupp, M., Rauball, J., and Tari, G., 2018, Paratethyan petroleum source rocks: An overview: Journal of Petroleum Geology, v. 41, p. 219–245, https://doi.org/10.1111/jpg.12702.

Sanei, H., Grasby, S.E., and Beauchamp, B., 2012, Latest Permian mercury anomalies: Geology, v. 40, p. 63–66, https://doi.org/10.1130/G32596.1.

Savian, J.F., Jovane, L., Frontalini, F., Trindade, R.I.F., Coccioni, R., Bohaty, S.M., Wilson, P.A., Florindo, F., Roberts, A.P., Catanzariti, R., and Iacoviello, F., 2014, Enhanced primary productivity and magnetotactic bacterial production in response to middle Eocene warming in the Neo-Tethys Ocean: Palaeogeography, Palaeoclimatology, Palaeoecology, v. 414, p. 32–45, https://doi.org/10.1016/j.palaeo.2014.08.009.

Schoepfer, S.D., Shen, J., Wei, H., Tyson, R.V., Ingall, E., and Algeo, T.J., 2015, Total organic carbon, organic phosphorus, and biogenic barium fluxes as proxies for paleomarine productivity: Earth-Science Reviews, v. 149, p. 23–52, https://doi.org/10.1016/j.earscirev.2014.08.017.

Schouten, S., Hopmans, E.C., Schefuß, E., and Sinninghe Damsté, J.S., 2002, Distributional variations in marine crenarchaeotal membrane lipids: A new tool for reconstructing ancient sea water temperatures?: Earth and Planetary Science Letters, v. 204, p. 265–274, https://doi.org/10.1016/S0012-821X(02)00979-2.

Schouten, S., Hopmans, E.C., and Sinninghe Damsté, J.S., 2013, The organic geochemistry of glycerol dialkyl glycerol tetraether lipids: A review: Organic Geochemistry, v. 54, p. 19–61, https://doi.org/10.1016/j.orggeochem.2012.09.006.

Schuster, P.F., Krabbenhoft, D.P., Naftz, D.L., Cecil, L.D., Olson, M.L., Dewild, J.F., Susong, D.D., Green, J.R., and Abbott, M.L., 2002, Atmospheric mercury deposition during the last 270 years: A glacial ice core record of natural and anthropogenic sources: Environmental Science & Technology, v. 36, p. 2303–2310, https://doi.org/10.1021/es0157503.

Scott, C., and Lyons, T.W., 2012, Contrasting molybdenum cycling and isotopic properties in euxinic versus non-euxinic sediments and sedimentary rocks: Refining the paleoproxies: Chemical Geology, v. 324–325, p. 19–27, https://doi.org/10.1016/j.chemgeo.2012.05.012.

Shcherbinina, E., Gavrilov, Y., Iakovleva, A., Pokrovsky, B., Golovanova, O., and Aleksandrova, G., 2016, Environmental dynamics during the Paleocene-Eocene thermal

maximum (PETM) in the northeastern Peri-Tethys revealed by high-resolution micropalaeontological and geochemical studies of a Caucasian key section: Palaeogeography, Palaeoclimatology, Palaeoecology, v. 456, p. 60–81, https://doi.org/10.1016/j.palaeo.2016.05.006.

Shen, J., Feng, Q., Algeo, T.J., Liu, J., Zhou, C., Wei, W., Liu, J., Them, T.R., Gill, B.C., and Chen, J., 2020, Sedimentary host phases of mercury (Hg) and implications for use of Hg as a volcanic proxy: Earth and Planetary Science Letters, v. 543, https://doi.org/10.1016/j.epsl.2020.116333.

Sluijs, A., Pross, J., and Brinkhuis, H., 2005, From greenhouse to icehouse: Organic-walled dinoflagellate cysts as paleoenvironmental indicators in the Paleogene: Earth-Science Reviews, v. 68, p. 281–315, https://doi.org/10.1016/j.earscirev.2004.06.001.

Sluijs, A., Zeebe, R.E., Bijl, P.K., and Bohaty, S.M., 2013, A middle Eocene carbon cycle conundrum: Nature Geoscience, v. 6, p. 429–434, https://doi.org/10.1038/ngeo1807.

Sluijs, A., Frieling, J., Inglis, G.N., Nierop, K.G.J., Peterse, F., Sangiorgi, F., and Schouten, S., 2020, Late Paleocene–early Eocene Arctic Ocean sea surface temperatures: Reassessing biomarker paleothermometry at Lomonosov Ridge: Climate of the Past, v. 16, p. 2381–2400, https://doi.org/10.5194/cp-16-2381-2020.

Spofforth, D.J.A., Agnini, C., Pälike, H., Rio, D., Fornaciari, E., Giusberti, L., Luciani, V., Lanci, L., and Muttoni, G., 2010, Organic carbon burial following the middle Eocene climatic optimum in the central western Tethys: Paleoceanography, v. 25, PA3210, https://doi.org/10.1029/2009PA001738.

Taylor, K.W.R., Huber, M., Hollis, C.J., Hernandez-Sanchez, M.T., and Pancost, R.D., 2013, Re-evaluating modern and Palaeogene GDGT distributions: Implications for SST reconstructions: Global and Planetary Change, v. 108, p. 158–174, https://doi.org/10.1016/j.gloplacha.2013.06.011.

Taylor, S.R. and McLennan, S.M., 1985, The Continental Crust: Its Composition and Evolution: Oxford, UK, Blackwell Scientific Publications, 312 p.

Thierstein, H.R., Geitzenauer, K.R., Molfino, B., and Shackleton, N.J., 1977, Global synchroneity of late Quaternary coccolith datum levels: Validation by oxygen isotopes: Geology, v. 5, p. 400–404, https://doi.org/10.1130/0091-7613(1977)5<400:GSOLQC>2.0.CO;2.

Thomson, J., Higgs, N.C., Wilson, T.R.S., Croudace, I.W., De Lange, G.J., and Van Santvoort, P.J.M., 1995, Redistribution and geochemical behaviour of redox-sensitive elements around S1, the most recent eastern Mediterranean sapropel: Geochimica et Cosmochimica Acta, v. 59, p. 3487–3501, https://doi.org/10.1016/0016-7037(95)00232-O.

Toffanin, F., Agnini, C., Rio, D., Acton, G., and Westerhold, T., 2013, Middle Eocene to early Oligocene calcareous nannofossil biostratigraphy at IODP Site U1333 (equatorial Pacific): Micropaleontology, v. 59, p. 69–82, https://doi.org/10.47894/mpal.59.1.04.

Tribovillard, N., Algeo, T.J., Lyons, T., and Riboulleau, A., 2006, Trace metals as paleoredox and paleoproductivity proxies: An update: Chemical Geology, v. 232, p. 12–32, https://doi.org/10.1016/j.chemgeo.2006.02.012.

van der Boon, A., van der Ploeg, R., Cramwinckel, M.J., Kuiper, K.F., Popov, S.V., Tabachnikova, I.P., Palcu, D.V., and Krijgsman, W., 2019, Integrated stratigraphy of the Eocene–Oligocene deposits of the northern Caucasus (Belaya River, Russia): Intermittent oxygen-depleted episodes in the Peri-Tethys and Paratethys: Palaeogeography, Palaeoclimatology, Palaeoecology, v. 536, https://doi.org/10.1016/j.palaeo.2019.109395.

van der Boon, A., Kuiper, K.F., van der Ploeg, R., Cramwinckel, M.J., Honarmand, M., Sluijs, A., and Krijgsman, W., 2021, Exploring a link between the middle Eocene climatic optimum and Neotethys continental arc flare-up: Climate of the Past, v. 17, p. 229–239, https://doi.org/10.5194/cp-17-229-2021.

van der Ploeg, R., Selby, D., Cramwinckel, M.J., Li, Y., Bohaty, S.M., Middelburg, J.J., and Sluijs, A., 2018, Middle Eocene greenhouse warming facilitated by diminished weathering feedback: Nature Communications, v. 9, p. 1–10, https://doi.org/10.1038/s41467-018-05104-9.

van Helmond, N.A.G.M., Ruvalcaba Baroni, I., Sluijs, A., Sinninghe Damsté, J.S., and Slomp, C.P., 2014, Spatial extent and degree of oxygen depletion in the deep proto–North Atlantic basin during oceanic anoxic event 2: Geochemistry Geophysics Geosystems, v. 15, p. 4254–4266, https://doi.org/10.1002/2014GC005528.

van Helmond, N.A.G.M., Jilbert, T., and Slomp, C.P., 2018, Hypoxia in the Holocene Baltic Sea: Comparing modern versus past intervals using sedimentary trace metals: Chemical Geology, v. 493, p. 478–490, https://doi.org/10.1016/j.chemgeo.2018.06.028.

van Hinsbergen, D.J.J., de Groot, L.V., van Schaik, S.J., Spakman, W., Bijl, P.K., Sluijs, A., Langereis, C.G., and Brinkhuis, H., 2015, A paleolatitude calculator for paleoclimate studies: PLoS One, v. 10, https://doi.org/10.1371/journal.pone.0126946.

Verdel, C., Wernicke, B.P., Hassanzadeh, J., and Guest, B., 2011, A Paleogene extensional arc flare-up in Iran: Tectonics, v. 30, TC3008, https://doi.org/10.1029/2010TC002809.

Wei, W., and Wise, S.W., 1989, Paleogene calcareous nannofossil magnetobiochronology: Results from South Atlantic DSDP Site 516: Marine Micropaleontology, v. 14, p. 119–152, https://doi.org/10.1016/0377-8398(89)90034-0.

Weijers, J.W.H., Lim, K.L.H., Aquilina, A., Sinninghe Damsté, J.S., and Pancost, R.D., 2011, Biogeochemical controls on glycerol dialkyl glycerol tetraether lipid distributions in sediments characterized by diffusive methane flux: Geochemistry Geophysics Geosystems, v. 12, Q10010, https://doi.org/10.1029/2011GC003724.

Westerhold, T., and Röhl, U., 2013, Orbital pacing of Eocene climate during the middle Eocene climate optimum and the chron C19r event: Missing link found in the tropical western Atlantic: Geochemistry Geophysics Geosystems, v. 14, p. 4811–4825, https://doi.org/10.1002/ggge.20293.

Westerhold, T., Marwan, N., Drury, A.J., Liebrand, D., Agnini, C., Anagnostou, E., Barnet, J.S.K., Bohaty, S.M., Vleeschouwer, D.D., Florindo, F., Frederichs, T., Hodell, D.A., Holbourn, A.E., Kroon, D., Lauretano, V., Littler, K., Lourens, L.J., Lyle, M., Pälike, H., Röhl, U., Tian, J., Wilkens, R.H., Wilson, P.A., and Zachos, J.C., 2020, An astronomically dated record of Earth's climate and its predictability over the last 66 million years: Science, v. 369, p. 1383–1387, https://doi.org/10.1126/science.aba6853.

Williams, G.L., Fensome, R.A., and MacRae, R.A., 2017, The Lentin and Williams Index of Fossil Dinoflagellates (2017 ed.): Dallas, Texas, American Association of Stratigraphic Palynologists Foundation, 1097 p.

Witt, M.L.I., Mather, T.A., Pyle, D.M., Aiuppa, A., Bagnato, E., and Tsanev, V.I., 2008, Mercury and halogen emissions from Masaya and Telica volcanoes, Nicaragua: Journal of Geophysical Research–Solid Earth, v. 113, B06203, https://doi.org/10.1029/2007JB005401.

Xie, S., Liu, X.-L., Schubotz, F., Wakeham, S.G., and Hinrichs, K.-U., 2014, Distribution of glycerol ether lipids in the oxygen minimum zone of the eastern tropical North Pacific Ocean: Organic Geochemistry, v. 71, p. 60–71, https://doi.org/10.1016/j.orggeochem.2014.04.006.

Zakrevskaya, E., Beniamovsky, V., Less, G., and Báldi-Beke, M., 2011, Integrated biostratigraphy of Eocene deposits in the Gubs section (northern Caucasus) with special attention to the Ypresian/Lutetian boundary and to the Peritethyan-Tethyan correlation: Turkish Journal of Earth Sciences, v. 20, p. 753–792.

Zeebe, R.E., Ridgwell, A., and Zachos, J.C., 2016, Anthropogenic carbon release rate unprecedented during the past 66 million years: Nature Geoscience, v. 9, p. 325–329, https://doi.org/10.1038/ngeo2681.

Zell, C., Kim, J.-H., Moreira-Turcq, P., Abril, G., Hopmans, E.C., Bonnet, M.-P., Sobrinho, R.L., and Damsté, J.S.S., 2013, Disentangling the origins of branched tetraether lipids and crenarchaeol in the lower Amazon River: Implications for GDGT-based proxies: Limnology and Oceanography, v. 58, p. 343–353, https://doi.org/10.4319/lo.2013.58.1.0343.

Zhang, Y.G., Zhang, C.L., Liu, X.-L., Li, L., Hinrichs, K.-U., and Noakes, J.E., 2011, Methane index: A tetraether archaeal lipid biomarker indicator for detecting the instability of marine gas hydrates: Earth and Planetary Science Letters, v. 307, p. 525–534, https://doi.org/10.1016/j.epsl.2011.05.031.

Zhang, Y.G., Pagani, M., and Wang, Z., 2016, Ring index: A new strategy to evaluate the integrity of TEX_{86} paleothermometry: Paleoceanography, v. 31, p. 220–232, https://doi.org/10.1002/2015PA002848.

Science Editor: Rob Strachan
Associate Editor: Rupsa Roy

Manuscript Received 11 August 2021
Revised Manuscript Received 12 February 2022
Manuscript Accepted 21 June 2022

Printed in the USA